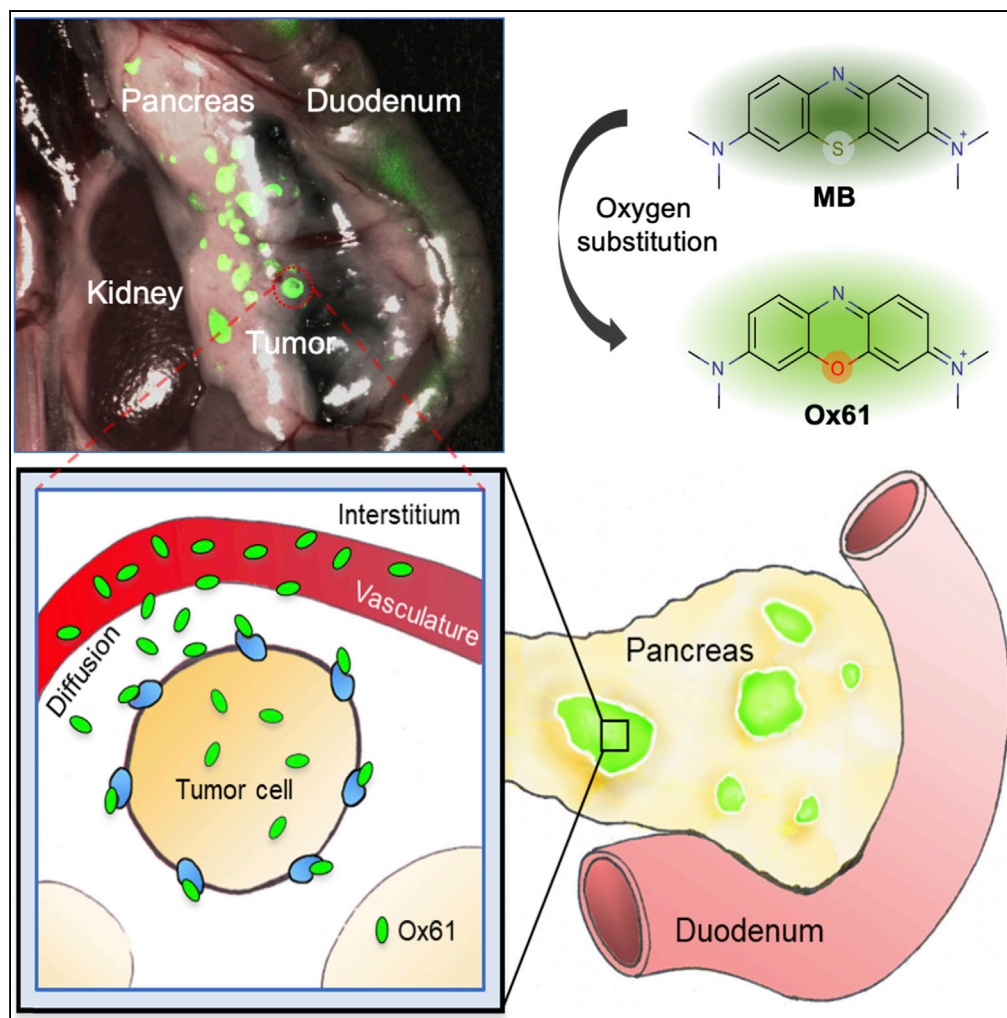


Article

Rapid and Selective Targeting of Heterogeneous Pancreatic Neuroendocrine Tumors



G. Kate Park,
Jeong Heon Lee,
Eduardo
Soriano, ...,
Satoshi Kashiwagi,
Maged Henary,
Hak Soo Choi

mhenary1@gsu.edu (M.H.)
hchoi12@mgh.harvard.edu
(H.S.C.)

HIGHLIGHTS

Bioengineered near-infrared fluorescent small molecules for PNET imaging

Highlight tumors within a minute after a single bolus injection with improved retention

Sensitive and specific detection of ultrasmall ectopic tumors

Intraoperative image-guided navigation provides a surgical margin

Park et al., iScience 23, 101006
April 24, 2020 © 2020 The
Author(s).
[https://doi.org/10.1016/
j.isci.2020.101006](https://doi.org/10.1016/j.isci.2020.101006)

Article

Rapid and Selective Targeting of Heterogeneous Pancreatic Neuroendocrine Tumors

G. Kate Park,^{1,7} Jeong Heon Lee,^{1,7} Eduardo Soriano,² Myunghwan Choi,³ Kai Bao,¹ Wataru Katagiri,¹ Do-Yeon Kim,⁴ Ji-Hye Paik,⁴ Seok-Hyun Yun,³ John V. Frangioni,⁵ Thomas E. Clancy,⁶ Satoshi Kashiwagi,¹ Maged Henary,^{2,*} and Hak Soo Choi^{1,8,*}

SUMMARY

Design of tissue-specific contrast agents to delineate tumors from background tissues is a major unmet clinical need for ultimate surgical interventions. Bioconjugation of fluorophore(s) to a ligand has been mainly used to target overexpressed receptors on tumors. However, the size of the final targeted ligand can be large, >20 kDa, and cannot readily cross the microvasculature to meet the specific tissue, resulting in low targetability with a high background. Here, we report a small and hydrophilic phenoxazine with high targetability and retention to pancreatic neuroendocrine tumor. This bioengineered fluorophore permits sensitive detection of ultrasmall (<0.5 mm) ectopic tumors within a few seconds after a single bolus injection, highlighting every tumor in the pancreas from the surrounding healthy tissues with reasonable half-life. The knowledge-based approach and validation used to develop structure-inherent tumor-targeted fluorophores have a tremendous potential to improve treatment outcome by providing definite tumor margins for image-guided surgery.

INTRODUCTION

An ideal tumor-targeted contrast agent should have high uptake and prolonged retention in malignant tissue as well as minimum uptake and fast clearance from surrounding normal tissues (Choi and Kim, 2020; Owens et al., 2015). The most common tumor targeting strategy is to conjugate a targeting ligand (e.g., small molecule, peptide, peptidomimetic, or protein) to a contrast agent (Choi et al., 2013). Targeted delivery of a specific agent to the cancerous tissue is significant for oncologists to plan a treatment strategy as well as for surgeons to decide the surgical margin based on image guidance (Kang et al., 2016, 2020).

The resection of pancreatic neuroendocrine tumor (PNET) and the avoidance of normal pancreas represent a significant unmet clinical need. Currently, intraoperative visual inspection and palpation performed by the surgeon is considered the most reliable source for PNET detection, which often results in incomplete resection of the tumor, with 5-year disease recurrence rate of 10% and 97% of patients without and with liver metastasis, respectively (Mayo et al., 2010; Lo et al., 1997; Mabrut et al., 2001; Ravi and Britton, 2007). Therefore, complete tumor resection remains the only treatment option that improves patient survival (Wong et al., 2018; Mayo et al., 2010).

Significant efforts have been focused on improving preoperative and intraoperative identification of tumors and their margins; however, it presents a major challenge to detect PNET with sufficient sensitivity (Grant, 2005; Galiber et al., 1988). Conventional preoperative techniques such as computed tomography (CT), magnetic resonance imaging (MRI), and endoscopic ultrasonography are successful in localizing larger tumors, although detection is very challenging for subcentimeter lesions with a broad-ranged sensitivity (9.6%–71%) (Galiber et al., 1988). Undetectable small-size PNET can cause severe symptoms of hormonal imbalance such as hypoglycemia or hyperglucagonemia due to excess production of insulin or glucagon, respectively. To increase small tumor detection, glucagon-like peptide-1 (GLP-1) radioligands were developed to diagnose PNET with highly expressed GLP-1 receptors on beta-cells, yet detecting tumors <2 cm remains elusive (Reiner et al., 2011; Wild et al., 2008).

Near-infrared (NIR) fluorescence imaging has the potential to improve the detectability and spatial resolution significantly (Hyun et al., 2014, 2015b; Owens et al., 2016). Currently, only two small NIR fluorophores,

¹Gordon Center for Medical Imaging, Department of Radiology, Massachusetts General Hospital and Harvard Medical School, Boston, MA 02114, USA

²Department of Chemistry, Center for Diagnostics and Therapeutics, Georgia State University, 100 Piedmont Ave SE, Atlanta, Georgia 30303, USA

³Wellman Center for Photomedicine, Massachusetts General Hospital and Harvard Medical School, MA 02139, USA

⁴Department of Pathology and Laboratory Medicine, Weill Cornell Medical College, New York, NY 10065, USA

⁵Curadel, LLC, Natick, MA 01760, USA

⁶Division of Surgical Oncology, Brigham and Women's Hospital and Dana-Farber Cancer Institute, Boston, MA 02215, USA

⁷These authors contributed equally

⁸Lead Contact

*Correspondence: mhenary1@gsu.edu (M.H.), hchoi12@mgh.harvard.edu (H.S.C.)

<https://doi.org/10.1016/j.isci.2020.101006>



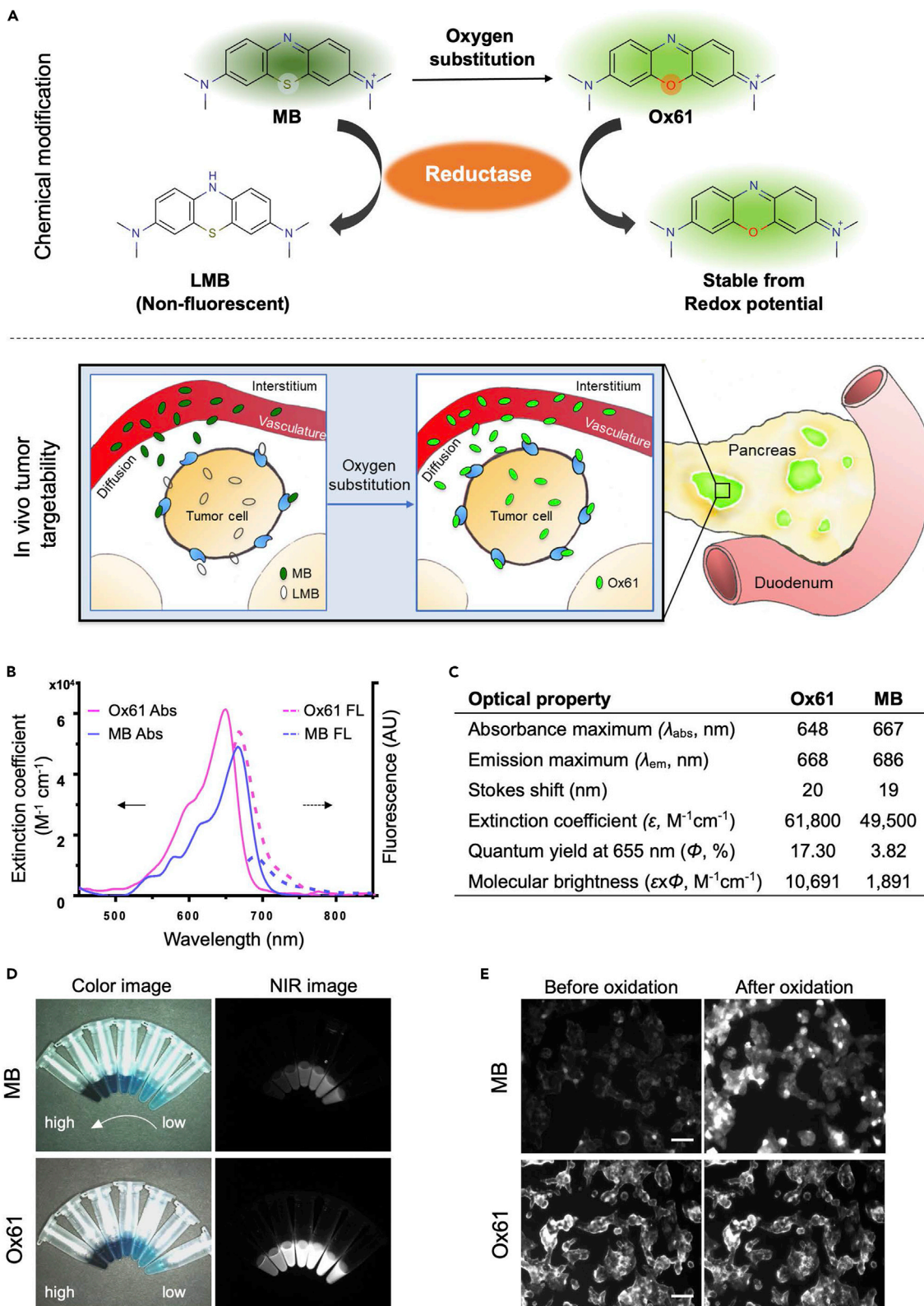


Figure 1. PNET-Specific Fluorescent Agents MB and Ox61

(A) Schematic drawing of PNET targeting by NIR fluorophores: MB converts to colorless leucomethylene blue (LMB) in erythrocytes, whereas oxygen substitution become inert from redox mechanisms in the body.
(B and C) (B) Comparison of optical properties: absorbance (solid line: left axis) and fluorescence emission (dotted line: right axis) spectra (C) optical properties measured in 100% serum, pH 7.0.
(D) Fluorescence imaging of difference concentration of MB and Ox61.
(E) Live cell binding assay: 2 μM of MB or Ox61 was incubated for 1 h with NIT-1 (pancreatic beta cell) and α -TC1 (pancreatic alpha cell) cell lines, followed by treatment with 0.1 mM of periodic acid to induce oxidation. Scale bar, 50 μm .

methylene blue (MB) and indocyanine green (ICG), have been FDA approved for tumor imaging in the clinics without clarifying the mode of action (Tummers et al., 2014; Alander et al., 2012), resulting in low tumor-to-background ratio (TBR). Previously, MB was used for detecting insulinoma, the most common functioning PNET, using optical imaging (Winer et al., 2010). However, due to its poor optical properties (i.e., low molecular brightness), rapid clearance from the body, and chemical reduction, MB is not ideal for intraoperative tumor targeting. Therefore, bioengineering of a single NIR small fluorophore to target such a tiny neoplasm is of significant importance with improved specificity and biodistribution (Hyun et al., 2015a; Choi, 2014).

The delivery and retention of a molecule in tumor tissue is dependent on the size, charge, hydrophobicity, pharmacodynamics, pharmacokinetics, and its transport across the tumor vasculature (Kang et al., 2018; Lee et al., 2012). However, the physicochemical properties of cancer-targeting fluorophores are not well established. In the present study, we have developed a lead PNET-targeted, phenoxazine-based NIR fluorescent contrast agent by analyzing the biodistribution of a small fluorophore library with the potentials to accumulate into PNET using insulinoma-bearing transgenic mice. Thereby, we have determined bioengineering of the physicochemical properties, and pharmacokinetics is required to achieve the specific targeting for PNET that can provide image guidance needed during the tumor resection.

RESULTS**Systemic Modification for Development of PNET Targeting NIR Fluorophore**

MB is the first and the only NIR fluorophore used for intraoperative localization of PNET (Winer et al., 2010). However, when MB is administrated intravenously into the body, approximately 75% is reduced to leuco-MB in erythrocytes via the endogenous reductase by consuming NADPH and loses fluorescence (May et al., 2003; Blazquez-Castro et al., 2009; Bradberry, 2003; Matsui et al., 2010). Despite these limitations of MB as an endocrine tumor imaging agent, we still believed that the core structure of the MB holds the key properties for the initial accumulation into the tumor and hypothesized that systematic modification of MB could potentially improve its optical and biological characteristics.

Therefore, we first focused on enhancement of optical properties and *in vivo* stability of MB. Among several different substitutions of the MB core (data not shown), we found that substitution of the sulfur atom of MB with oxygen resulted in the most improvement in both optical and biological properties (Figure 1A). With this first modification, we named the molecule Ox61 (see Transparent Methods and Figures S1–S5). The single oxygen substitution in Ox61 led to hypsochromic shift and 5.7-fold brightness increase compared with MB: 1.3-fold increase in molecular absorbance ($\Delta\epsilon = 12,300 \text{ M}^{-1}\text{cm}^{-1}$) and 4.5-fold increase in quantum yield ($\Delta\Phi = 8.6\%$), respectively (Figures 1B–1D) (Bradberry, 2003).

To show high redox stability toward biological reduction after oxygen substitution, we performed an *in vitro* live cell assay to evaluate the cellular specificity by comparing MB and Ox61 in NIT-1 (pancreatic β -cell). Both MB and Ox61 stained the NIT-1 cells; however, Ox61 showed a significantly higher signal compared with MB (Figure 1E, $P < 0.05$). We subsequently treated the membrane-stained cells with 0.1 mM periodic acid to test the presence of the leuco form of both fluorophores. Interestingly, the fluorescence signal of MB inside NIT-1 cells was recovered by oxidation, whereas no notable changes were observed in the Ox61 stained cells, which remained high pre- and post-treatment. Similarly, we also treated periodic acid on the kidneys resected from normal CD-1 mice 1 h after injecting 1.5 mg/kg of MB or Ox61 intravenously. The fluorescence signal significantly increased in the MB-injected mouse kidney, whereas no intensity changes were found in the Ox61-injected mouse kidney (Figure S6, $P < 0.0001$). This indicates that MB is reduced to LMB by endogenous reductase, but Ox61 is stable from the redox cycle and retains strong fluorescence signal.

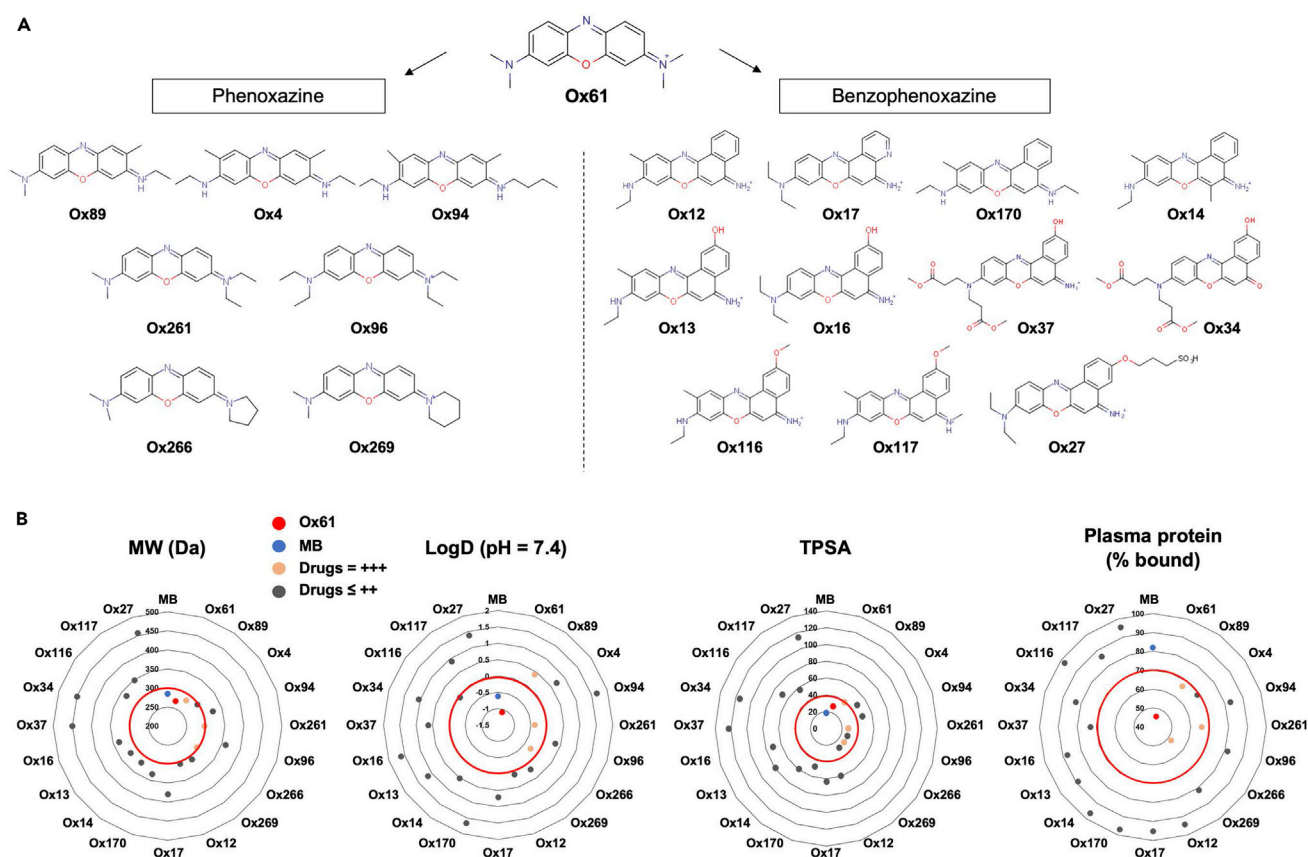


Figure 2. PNET-Specific Fluorescent Small Molecule Library

(A) Molecular structure of PNET-specific fluorophores.

(B) Quantitative calculation of molecular weight (MW), logD, TPSA, and plasma protein % bound.

Structural Characterization of PNET Targeting NIR Fluorophore

After the first modification and the improvement in optical properties and biological stability, we then synthesized 18 additional phenoxazine derivatives by varying side chains (Figure 2A). To test the tumor targetability of these derivatives, 1.5 mg/kg of each molecule was injected intravenously into the insulinoma bearing mice and imaged 30 min after injection under the FLARE intraoperative optical imaging system (Figure S7A) (Gioux et al., 2010). Physicochemical properties and tumor-to-background ratio (Tu/Pa) of MB and molecules in PNET library are summarized in Table 1. Among the 19 contrast agents, four (Ox61, 89, 261, and 266) had TBR >2.0 and only Ox61 had TBR >5.0. We then analyzed the quantitative physicochemical properties of the molecules to define the criteria required for PNET targetability. Molecular weight (MW), hydrophobicity, and total polar surface area of each agent were plotted in a chart, and Ox61 was labeled with red (TBR >5.0), MB with blue, molecules with TBR above 2 with orange, and the rest with dark gray (Figure 2B). Based on the chart, we were able to determine the PNET targetability range for each chemical property (red margin), and if the molecule did not fall within the optimal range, it had low or no tumor targetability. In summary, highly hydrophilic molecules with low molecular weight (<300 Da) and low TPSA (<40) had suitable accumulation in PNET. In addition, positive charge of the molecule favored tumor accumulation. Another interesting observation was that change in hydrophobicity of the molecule with elongation of side chain dramatically altered tumor targetability (Figure S7B). Other critical factors influencing tumor targeting are the plasma pharmacokinetics of probe residence in the circulation and diffusivity of the molecule across tumor vasculature into the extravascular tissue^{25,26} (Dewhirst and Secomb, 2017). To evaluate the probe transport in circulation, we performed plasma protein binding test using the rapid equilibrium dialysis (RED) to determine the free (%Fu) and bound (%Bound) fraction of drugs in plasma. As a result, Ox61 with the highest tumor uptake had the least plasma protein bound fraction (45% bound) and the Ox89, 261, and 266 with TBR around 2 also had (<50%–70% bound), which is relatively low compared with the rest of the drugs with low or no tumor uptake (90%–100% bound) (Table 1,

Drug	MW (g/mol)	Log D (pH = 7.4)	TPSA (Å ²)	HBA	Volume (Å ³)	Dipole (Debye)	Polarizability (Cm ² V ⁻¹)	Plasma (% Bound)	Tumor Intensity
MB	284.40	-0.62	18.61	2	387.92	9.48	32.74	81.92	+++
Ox61	268.34	-1.09	27.84	3	382.04	9.38	30.34	45.87	+++++
Ox89	282.37	0.41	38.80	3	414.96	10.39	32.18	66.59	+++
Ox261	296.39	-0.38	27.84	3	447.63	8.24	34.03	65.82	+++
Ox266	294.38	-0.27	27.84	3	420.29	7.97	33.30	52.01	+++
Ox4	296.40	0.70	47.59	3	442.88	10.87	33.95	68.84	++
Ox14	318.40	0.51	59.21	3	449.60	9.66	36.39	96.42	++
Ox17	379.39	0.71	63.31	4	442.36	10.46	35.57	95.06	++
Ox94	324.45	1.66	47.59	3	504.25	7.79	37.64	82.91	++
Ox12	304.37	0.09	59.21	3	416.51	10.37	34.55	94.22	+
Ox116	334.40	-0.06	68.44	4	434.52	11.43	37.06	97.73	+
Ox117	348.43	0.91	56.82	4	499.17	10.22	38.90	86.13	+
Ox170	332.43	1.65	47.59	3	483.61	8.64	38.24	96.92	+
Ox269	308.40	0.18	27.84	3	447.78	7.00	35.14	81.28	+
Ox13	320.37	1.15	79.44	4	427.66	9.80	35.14	88.98	-
Ox16	334.40	1.62	70.65	4	460.05	12.80	37.06	87.62	-
Ox27	456.54	1.38	114.02	7	631.86	11.87	47.30	95.48	-
Ox37	450.17	0.63	123.25	6	606.75	22.07	46.00	73.12	-
Ox34	450.45	1.05	114.73	7	604.36	11.90	45.08	82.91	-
Ox96	324.45	0.33	27.84	3	508.56	74.72	37.72	81.45	-

Table 1. In Silico Physicochemical Properties of PNET-Targeted Contrast Agents

MW, molecular weight; TPSA, total polar surface area; HBA, hydrogen bond acceptors. Tumor to background ratio (TBR) against normal pancreas was quantified and labeled as -, <1; +, 1-2; ++, 2-3; +++, 3-4; +++++, >5.

Figure 2B). These results indicate that low plasma binding favors tumor targeting, which would prevent sequestration of a probe to plasma compartment.

Kinetics and Dose Dependence of Ox61

Because MB is the only available PNET contrast agent, we compared results directly obtained with the lead compound Ox61 with MB. We first compared *in vivo* biodistribution and clearance pattern in normal CD-1 mice 4 h after a single intravenous injection of Ox61 or MB (Figure S8). The pattern for biodistribution and renal excretion was almost identical, but the fluorescence signal in the Ox61 injected mice was about 2- to 5-fold higher than MB injected mice. We also compared *in vivo* biodistribution and blood clearance and found that Ox61 had prolonged blood circulation compared with MB. In these comparisons, we excluded the measurement of leuco-MB form to make a direct comparison with Ox61 for their *in vivo* fluorescence signals. The elimination blood half-life ($t_{1/2\beta}$) of Ox61 was 3-fold longer than that of MB (47 versus 15 min) in mice (Figure 3A). We next performed a wide range of dose tests between 0.3 and 6.0 mg/kg. Although the lowest dose of 0.3 mg/kg resulted in improved TBR compared with MB, substantial signal increase in tumors occurred with 1.5 mg/kg and 3.0 mg/kg of Ox61, which showed much higher TBR compared with MB (Figure 3B, $P < 0.001$). Tumor signals were further increased when injected with the maximum dose of 6.0 mg/kg, but the background signal in pancreas also increased, which lowered the TBR between 1 h and 4 h. To determine the optimum time point for tumor targeting, we injected 1.5 mg/kg of Ox61 or MB into insulinoma-bearing mice and observed the TBR change over 4 h post-injection. In both cases, tumors became bright immediately after injection (Figure 3C). However, the pattern of uptake and retention at the tumorous tissue was notably different between Ox61 and MB. Ox61

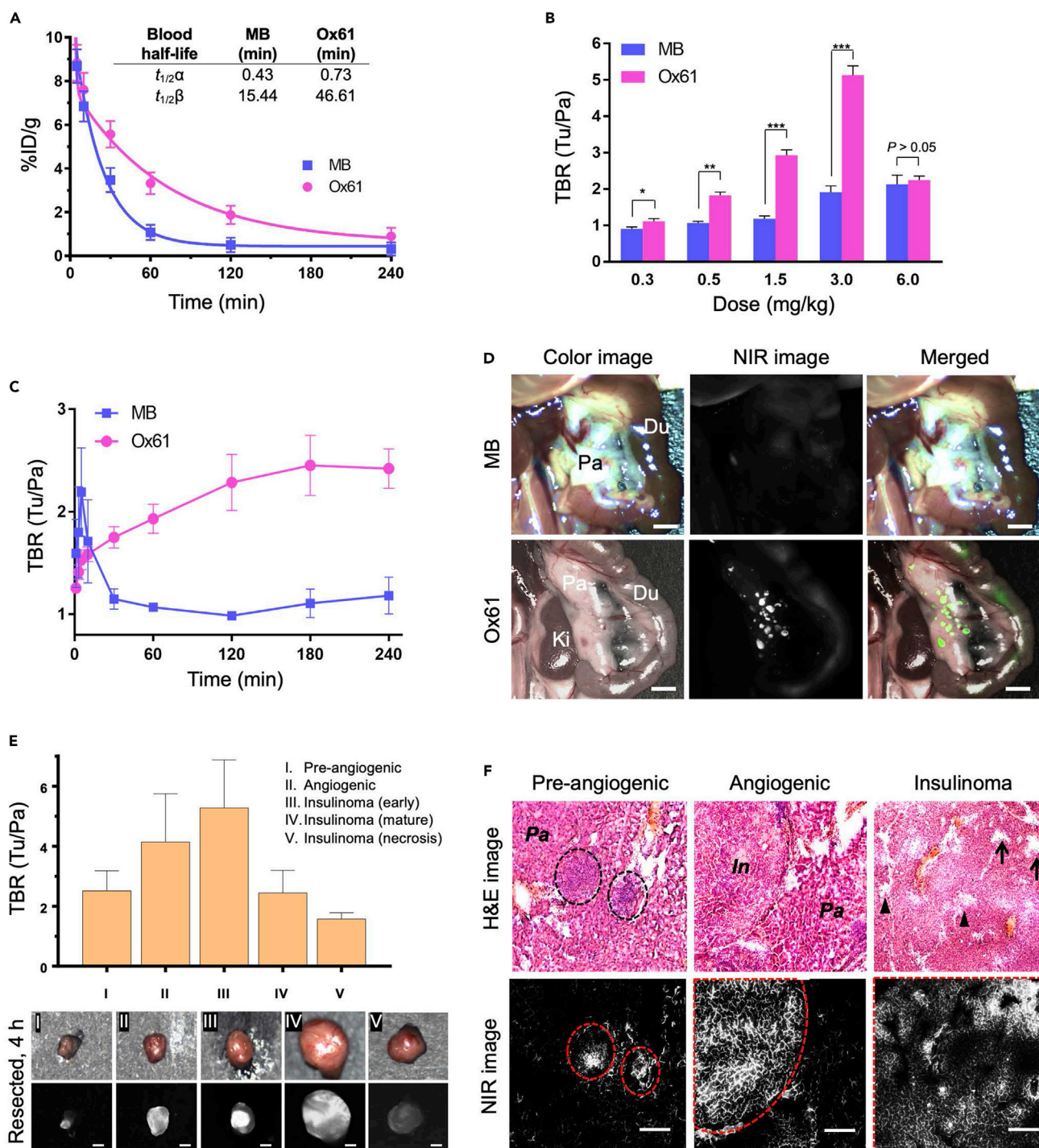


Figure 3. Intraoperative Imaging and Image-Guided Resection of PNET

(A) Blood half-life (%ID/g) of each compound in mice was calculated using the nonlinear regression two-phase exponential decay method.
 (B) Dose-response curve of TBR (mean \pm SEM) for MB (blue) and Ox61 (red). Different doses of each fluorophore were injected intravenously into insulinoma mice, and TBR (Tu/Pa) was quantified.
 (C) Quantitative time course assessment of TBR (mean \pm SEM) for MB (blue) and Ox61 (red) for 4 h after a single bolus injection (1.5 mg/kg) of each fluorophore.
 (D) 1.5 mg/kg of MB or Ox61 was injected into 14-week-old insulinoma-bearing mice 4 h prior to imaging. Shown are occult and ectopic tumor metastases using NIR fluorescence.

Figure 3. Continued

(E) Image-guided tumor resection after intraoperative tumor imaging and tumors at each stage were resected 4 h post-injection of Ox61 (1.5 mg/kg) and quantified ($n = 5$, mean \pm s.d.). All NIR fluorescence images for each condition have identical exposure times and normalizations. Scale bars, 1 mm. (F) Histological evaluation of different stages of tumors in insulinoma-bearing pancreas. Shown are H&E and 700 nm NIR fluorescence (Ox61) of three different stages of resected tumors. Insulinoma stage of tumor showed presence of normal (arrow) and squeezed (arrowhead) vasculature. All NIR fluorescence images for each condition have identical exposure times and normalizations. I, insulinoma; E, exocrine pancreas. Scale bars, 100 μ m

gradually accumulated into insulinomas over 3 h post-injection, whereas MB rapidly disappeared within 1 h. The peak TBR of Ox61 occurred 3–4 h post-intravenous injection, at which point surrounding background signal had decreased drastically.

Tumor Targetability and Specificity of Ox61

Having determined optimal kinetics and dose, we tested the effect of physiological changes from tumor developmental stage on Ox61 uptake and retention. Small occult PNET (<2 mm) are extremely difficult to localize and cannot typically be visualized in the surgical field. When insulinoma-bearing mice were injected with Ox61, however, small occult tumors were clearly visualized throughout the pancreas (Video S1). In contrast, similar tumors were not detectable at 4 h post-injection of MB because of its fast elimination, leuco-MB formation, and poor optical properties (Figure 3D). After a single intravenous injection of Ox61, we successfully resected five different developmental stages of tumorigenesis under fluorescence image guidance with high TBR (tumor to pancreas) (Figure 3E). Because MRI has been used previously to monitor tumor growth, we compared tumor detectability with intraoperative fluorescence imaging. MRI visualized both hyperintense (early stage) and isointense (late stage) of larger sized tumors (>2 mm) of 13-week-old insulinoma mouse, yet delineating tumor margins was a challenge. After injection of 1.5 mg/kg of Ox61 into the same mouse, we obtained intraoperative fluorescence images co-registered with the MR images (Figure S9A). Dual-modality imaging permitted clearer margin assessment; however, fluorescence imaging revealed additional small tumors that were not detectable by MRI.

Next, we tested the effect of physiological change in tumor stages on Ox61 accumulation. PNET stages are well defined in transgenic mice: pre-angiogenic/hyperplasia (5–6 weeks), angiogenic/dysplasia (7–9 weeks), early stage tumors (10–11 weeks), mature stage tumors (11–13 weeks), and necrotic tumors (>13 weeks) (Bergers et al., 1999). We performed Ox61-based tumor imaging in 5- to 13-week-old insulinoma-bearing mice (Figure S9B). Surprisingly, Ox61 was able to target and localize pre-angiogenic tumors in mice with a reliable TBR ≥ 2.0 but short retention time compared with angiogenic and tumor stage. Histopathologic evaluation was performed on resected tumor tissues, which confirmed the morphological changes of tumors at each stage (Figure 3F). Despite the heterogeneity nature of pancreatic endocrine tumorigenesis, the efficient uptake of Ox61 at all stages of tumors was observed. Hyperplasia stage and angiogenic stage tissues showed homogeneous fluorescence signal at the tumor site, whereas Ox61 uptake in the late stage of PNET was heterogeneous because, presumably, of limited blood supply. Areas around open vasculature exhibited more favorable accumulation of Ox61 compared with other areas with compressed vasculature (arrowheads).

Physiological Mechanism of Action of Ox61

To better understand the physiological mechanism of Ox61 accumulation at the tumor site, we measured absolute fluorescence intensity at the pancreas and the tumor from 0 to 150 s post-injection of 1.5 mg/kg of Ox61 and corresponding images at four different time points on the graph (Figure 4A). The entire pancreas and its associated tumors were stained with high intensity immediately after the injection. Both pancreas and tumors showed decrease in signal after reaching the peak of the blood distribution phase (phase 2). Interestingly, the signal intensity in the tumor increased gradually after a short period of clearance, whereas the pancreas signal continued to decrease (phase 3–4). This phenomenon clearly demonstrates the high specificity of Ox61 to tumor site. The distribution of tumor-targeting probe is dependent on the transport through tumor vasculature into the extravascular tissue (Dewhirst and Secomb, 2017). For further analysis of the diffusion of the Ox61 from the tumor capillaries, we performed real-time, quantitative intravital fluorescence imaging. Within 10 s after the injection a large amount of Ox61 diffused from microvasculature of the tumor followed by rapid accumulation in all tumorous tissues as well as large venules (Figure 4B). We next compared the performance of Ox61 with various tumor-specific protein-conjugated fluorophores (GLP-1, cRGDyK, and CREKA micelle, see Transparent Methods), which are known to have high specificity to tumors (Choi et al., 2013; Wild et al., 2008; Ruoslahti et al., 2010). None of these conjugates were able to target a single tumor in insulinoma-bearing mice 1 h post-injection (Figure S10A). In addition, we tested tumor cell specificity of Ox61 by generating NIT-1 subcutaneous tumor in nude mice and injected with 1.5 mg/kg of Ox61 but were not able to observe accumulation into the tumor (Figure S10B).

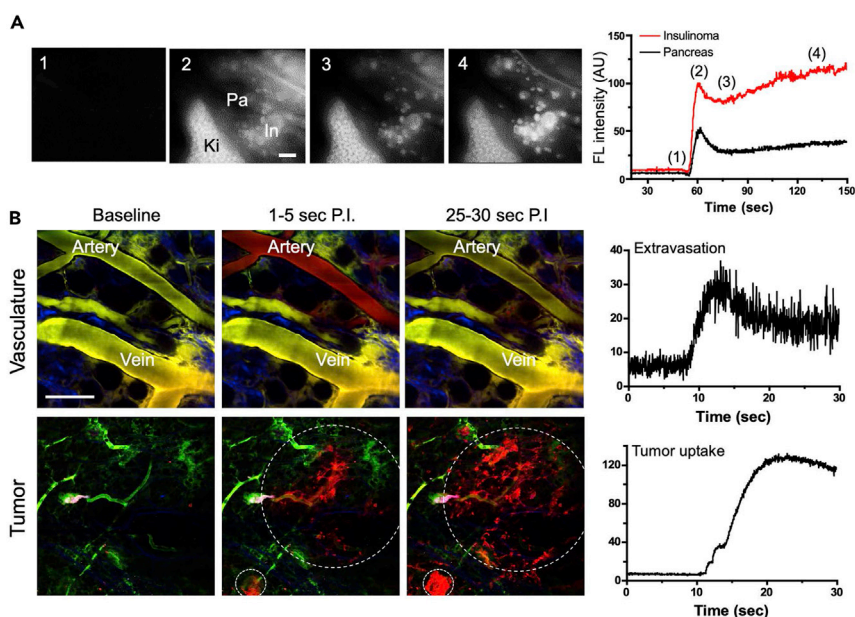


Figure 4. Extravasation and Tumor Uptake of Ox61 across Tumor Microvasculature

(A) Kinetics and representative intraoperative images for signal uptake in pancreas and PNET: (1) pre-injection, (2) circulation, (3) initial uptake, and (4) accumulation and retention. In, intestine; Ki, kidneys; Pa, pancreas.

(B) Representative intravital microscopic images with real-time quantification of the extravasation rate after a single intravenous injection of Ox61. Microvasculature was labeled with FITC-dextran (green color) 10 min prior to intravenous injection of Ox61 (red color). White dotted circles indicate PNET; scale bar, 200 μ m.

DISCUSSION

We have successfully developed a pancreatic tumor-targeted contrast agent, Ox61, through systemic engineering of a clinically available, yet poorly performing NIR fluorophore, MB, for intraoperative imaging (Winer et al., 2010; Matsui et al., 2010). Ox61 has overcome historical shortcomings of NIR fluorophores, including low water solubility, short circulation time, low quantum efficiencies, poor photostability, high plasma protein binding rate, and low TBR (Choi and Frangioni, 2010). Ox61 has improved molecular brightness (>5-fold), redox stability, blood circulation (>3-fold), and targeting specificity (>10-fold) compared with MB. The improvement in optical properties resulted from (1) high oscillator strength derived from the larger atom size (covalent radius of atom: S = 0.104 nm versus O = 0.066 nm), (2) low-energy π - π^* transition donating electron density (electronegativity: S = 2.4 versus O = 3.5), and (3) low solvation energies in polar media (HBA: S = 2 versus O = 3) (Bradberry, 2003).

Our data clearly indicate that design of a tumor-targeting fluorophore requires a specific combination of physicochemical properties of the molecule. By analyzing quantitative physicochemical properties of synthesized molecules (Figure 2A), we have determined that specificity to tumor is highly dependent on the chemical structure, MW, hydrophilicity ($\log D$ at pH 7.4), and total polar surface charge (Figure S8) (Lee et al., 2012). Molecular weight was a critical property because molecules larger than 300 Da had poor targetability. Hydrophilicity of molecule also played important role in determining tumor specificity; for example, elongation of one or two methyl groups on the side chain increased $\log D$ and decreased the tumor targetability. These physicochemical properties had combinatorial effect on the tumor targetability. MW less than 300 Da did not always have good tumor targetability if it also had high $\log D$ (Ox4). Also, if the molecule had slightly high $\log D$ with low TPSA and MW (Ox89), it likely also displayed good tumor targetability.

The distribution of tumor-targeting agents also relies on the plasma pharmacokinetics and transport through tumor vasculature into the extravascular tumor tissue (Dewhirst and Secomb, 2017). Plasma protein binding (PPB) greatly impacts the behavior (distribution and elimination) of the drug, where only the unbound fraction is available to interact with the target site (Trainor, 2007). To have lasting pharmacological effect, a large fraction of the drug must be distributed to the tumorous tissue with high affinity (Dewhirst and Secomb, 2017). Interestingly, Ox61 had the highest unbound fraction compared with all the other drugs in the library. In addition, molecules with similar physicochemical properties as Ox61 but lower TBR had smaller unbound fraction compared

with Ox61. This clearly explained why Ox61 outperformed all the other drugs and emphasize that PPB is a critical parameter to determine the availability of drug to the biological target.

Our data clearly show that Ox61 quickly extravasated and accumulated into tumor tissue with higher affinity compared with normal pancreas after intravenous injection (Figure 4). Physicochemical and pharmacodynamic characteristics including positive charge of Ox61 might facilitate extravasation and accumulation in tumor tissue with the negative charges of the vessel luminal face and molecules in the interstitial space (Campbell et al., 2002; Azzi et al., 2013). The development of targeted NIR fluorescent contrast agents for endocrine tumor is particularly difficult because it requires initial distribution into the endocrine organ while simultaneously localize in higher concentration within the targeting tumor, regardless of anatomic location and barriers to give contrast between the normal tissue (Hyun et al., 2014, 2015b; Owens et al., 2016). When bioengineering contrast agents that target tumors by their inherent chemical structures, we must determine the design criteria (i.e., size, charge, and hydrophobicity) of the drug with regard to the plasma pharmacokinetics and physiological barriers to the target tissue. A significant portion of Ox61 injected intravenously in a single formulation was immediately delivered to the tumors, providing unparalleled contrast between the normal pancreas and the pancreatic tumor. To our knowledge, there is no single contrast agent that can highlight tumor within a minute after intravenous injection.

In conclusion, NIR fluorescent intraoperative imaging using Ox61 greatly facilitated the localization of small occult PNET and has the potential to reduce operation times and increase the likelihood of negative margins. Our new technology of drug design for delivering targeted agent can be applied for developing various other tumor targeting agents (i.e., ovarian, breast, thyroid) and can result in immediate detection of tumor upon injection with high specificity, which is difficult to achieve with nanoparticles or proteins and transporter targeting. Furthermore, Ox61 has high potential for accelerated approval by FDA for clinical use of tumor targeting, following the safety and regulatory guideline of MB.

Limitation of the Study

Even though we performed extensive *in vivo* and molecular analyses to determine to the mechanism of action allowing PNET targeting by Ox61, we were unable to determine target proteins or transporters on PNET cells. The physicochemical properties of Ox61 led rapid molecular distribution into the tumor site, whereas the retention mechanism on the target needs further investigation.

METHODS

All methods can be found in the accompanying [Transparent Methods supplemental file](#).

SUPPLEMENTAL INFORMATION

Supplemental Information can be found online at <https://doi.org/10.1016/j.isci.2020.101006>.

ACKNOWLEDGMENTS

We thank Ivey Choi and Matt Laramie for manuscript editing. This study was supported by US NIH grants NIBIB #R01EB011523 and #R01EB022230 and the Georgia Research Alliance for the Ventures Phase 1 Grant. This work was also supported by the Joint Research Project for Outstanding Research Institutions funded by the Gimhae Industry Promotion and Biomedical Foundation, the Health Technology R&D Project #HI19C0166 funded by the Ministry of Health and Welfare, South Korea. The content expressed is solely the responsibility of the authors and does not necessarily represent the official views of the NIH.

AUTHOR CONTRIBUTIONS

GKP, JHL, SK, ES, KB, MC, WK, and DYK performed the experiments. GKP, JHL, SK, SHY, JHP, JVF, MH, and HSC reviewed, analyzed, and interpreted the data. GKP, JHL, SK, SHY, JHP, JVF, TEC, MH, and HSC wrote the paper. All authors discussed the results and commented on the manuscript.

DECLARATION OF INTERESTS

Dr. Frangioni is currently CEO of Curadel, LLC, a for-profit company that has licensed FLARE technology from Beth Israel Deaconess Medical Center.

Received: September 2, 2019

Revised: February 10, 2020

Accepted: March 18, 2020

Published: April 24, 2020

REFERENCES

- Alander, J.T., Kaartinen, I., Laakso, A., Patila, T., Spillmann, T., Tuchin, V.V., Venermo, M., and Valisuo, P. (2012). A review of indocyanine green fluorescent imaging in surgery. *Int. J. Biomed. Imaging* 2012, 940585.
- Azzi, S., Hebda, J.K., and Gavard, J. (2013). Vascular permeability and drug delivery in cancers. *Front. Oncol.* 3, 211.
- Bergers, G., Javaherian, K., Lo, K.M., Folkman, J., and Hanahan, D. (1999). Effects of angiogenesis inhibitors on multistage carcinogenesis in mice. *Science* 284, 808–812.
- Blazquez-Castro, A., Stockert, J.C., Sanz-Rodriguez, F., Zamarron, A., and Juarraz, A. (2009). Differential photodynamic response of cultured cells to methylene blue and toluidine blue: role of dark redox processes. *Photochem. Photobiol. Sci.* 8, 371–376.
- Bradberry, S.M. (2003). Occupational methaemoglobinemia. Mechanisms of production, features, diagnosis and management including the use of methylene blue. *Toxicol. Rev.* 22, 13–27.
- Campbell, R.B., Fukumura, D., Brown, E.B., Mazzola, L.M., Izumi, Y., Jain, R.K., Torchilin, V.P., and Munn, L.L. (2002). Cationic charge determines the distribution of liposomes between the vascular and extravascular compartments of tumors. *Cancer Res.* 62, 6831–6836.
- Choi, H.S. (2014). Nanoparticle assembly: building blocks for tumour delivery. *Nat. Nanotechnol.* 9, 93–94.
- Choi, H.S., and Frangioni, J.V. (2010). Nanoparticles for biomedical imaging: fundamentals of clinical translation. *Mol. Imaging* 9, 291–310.
- Choi, H.S., Gibbs, S.L., Lee, J.H., Kim, S.H., Ashitate, Y., Liu, F., Hyun, H., Park, G., Xie, Y., Bae, S., et al. (2013). Targeted zwitterionic near-infrared fluorophores for improved optical imaging. *Nat. Biotechnol.* 31, 148–153.
- Choi, H.S., and Kim, H.K. (2020). Multispectral image-guided surgery in patients. *Nat. Biomed. Eng.* 4, 245–246.
- Dewhirst, M.W., and Secomb, T.W. (2017). Transport of drugs from blood vessels to tumour tissue. *Nat. Rev. Cancer* 17, 738–750.
- Galiber, A.K., Reading, C.C., Charboneau, J.W., Sheedy, P.F., 2nd, James, E.M., Gorman, B., Grant, C.S., Van Heerden, J.A., and Teland, R.L. (1988). Localization of pancreatic insulinoma: comparison of pre- and intraoperative US with CT and angiography. *Radiology* 166, 405–408.
- Gioux, S., Choi, H.S., and Frangioni, J.V. (2010). Image-guided surgery using invisible near-infrared light: fundamentals of clinical translation. *Mol. Imaging* 9, 237–255.
- Grant, C.S. (2005). Insulinoma. *Best Pract. Res. Clin. Gastroenterol.* 19, 783–798.
- Hyun, H., Park, M.H., Owens, E.A., Wada, H., Henary, M., Handgraaf, H.J., Vahrmeijer, A.L., Frangioni, J.V., and Choi, H.S. (2015a). Structure-inherent targeting of near-infrared fluorophores for parathyroid and thyroid gland imaging. *Nat. Med.* 21, 192–197.
- Hyun, H., Park, M.H., Owens, E.A., Wada, H., Henary, M., Handgraaf, H.J.M., Vahrmeijer, A.L., Frangioni, J.V., and Choi, H.S. (2015b). Structure-inherent targeting of NIR fluorophores for parathyroid and thyroid gland imaging. *Nat. Med.* 21, 192–197.
- Hyun, H., Wada, H.K., Gravier, J., Yadav, Y., Laramie, M., Henary, M., Frangioni, J.V., and Choi, H.S. (2014). Phosphonated near-infrared fluorophores for biomedical imaging of bone. *Angew. Chem. Int. Ed.* 53, 10668–10672.
- Kang, H., Gravier, J., Bao, K., Wada, H., Lee, J.H., Baek, Y., El Fakhri, G., Gioux, S., Rubin, B.P., Coll, J.L., and Choi, H.S. (2016). Renal clearable organic nanocarriers for bioimaging and drug delivery. *Adv. Mater.* 28, 8162–8168.
- Kang, H., Hu, S., Cho, M.H., Hong, S.H., Choi, Y., and Choi, H.S. (2018). Theranostic nanosystems for targeted cancer therapy. *Nano Today* 23, 59–72.
- Kang, H., Stiles, W.R., Baek, Y., Nomura, S., Bao, K., Hu, S., Park, G.K., Jo, M.J., I, H., Coll, J.L., et al. (2020). Renal clearable theranostic nanoplateforms for gastrointestinal stromal tumors. *Adv. Mater.* 32, e1905899.
- Lee, J.H., Park, G., Hong, G.H., Choi, J., and Choi, H.S. (2012). Design considerations for targeted optical contrast agents. *Quant. Imaging Med. Surg.* 2, 266–273.
- Lo, C.Y., Lam, K.Y., Kung, A.W., Lam, K.S., Tung, P.H., and Fan, S.T. (1997). Pancreatic insulinomas. A 15-year experience. *Arch. Surg.* 132, 926–930.
- Mabrut, J.Y., Lifante, J.C., Cherki, S., Sin, S., Berger, N., and Peix, J.L. (2001). [Is preoperative localization of insulinomas necessary?]. *Ann. Chir.* 126, 850–856.
- Matsui, A., Tanaka, E., Choi, H.S., Kianzad, V., Gioux, S., Lomnes, S.J., and Frangioni, J.V. (2010). Real-time, near-infrared, fluorescence-guided identification of the ureters using methylene blue. *Surgery* 148, 78–86.
- May, J.M., Qu, Z.C., and Whitesell, R.R. (2003). Generation of oxidant stress in cultured endothelial cells by methylene blue: protective effects of glucose and ascorbic acid. *Biochem. Pharmacol.* 66, 777–784.
- Mayo, S.C., De Jong, M.C., Pulitano, C., Clary, B.M., Reddy, S.K., Gambin, T.C., Celinski, S.A., Kooby, D.A., Staley, C.A., Stokes, J.B., et al. (2010). Surgical management of hepatic neuroendocrine tumor metastasis: results from an international multi-institutional analysis. *Ann. Surg. Oncol.* 17, 3129–3136.
- Owens, E.A., Henary, M., El Fakhri, G., and Choi, H.S. (2016). Tissue-specific near-infrared fluorescence imaging. *Acc. Chem. Res.* 49, 1731–1740.
- Owens, E.A., Lee, S., Choi, J., Henary, M., and Choi, H.S. (2015). NIR fluorescent small molecules for intraoperative imaging. *Wiley Interdiscip. Rev. Nanomed. Nanobiotechnol.* 7, 828–838.
- Ravi, K., and Britton, B.J. (2007). Surgical approach to insulinomas: are pre-operative localisation tests necessary? *Ann. R. Coll. Surg. Engl.* 89, 212–217.
- Reiner, T., Thurber, G., Gaglia, J., Vinegoni, C., Liew, C.W., Upadhyay, R., Kohler, R.H., Li, L., Kulkarni, R.N., Benoist, C., et al. (2011). Accurate measurement of pancreatic islet beta-cell mass using a second-generation fluorescent extendin-4 analog. *Proc. Natl. Acad. Sci. U S A* 108, 12815–12820.
- Ruoslahti, E., Bhatia, S.N., and Sailor, M.J. (2010). Targeting of drugs and nanoparticles to tumors. *J. Cell. Biol.* 188, 759–768.
- Trainor, G.L. (2007). The importance of plasma protein binding in drug discovery. *Expert Opin. Drug Discov.* 2, 51–64.
- Tummers, Q.R., Verbeek, F.P., Schaafsma, B.E., Boonstra, M.C., Van Der Vorst, J.R., Liefers, G.J., Van De Velde, C.J., Frangioni, J.V., and Vahrmeijer, A.L. (2014). Real-time intraoperative detection of breast cancer using near-infrared fluorescence imaging and Methylene Blue. *Eur. J. Surg. Oncol.* 40, 850–858.
- Wild, D., Macke, H., Christ, E., Gloor, B., and Reubi, J.C. (2008). Glucagon-like peptide 1-receptor scans to localize occult insulinomas. *N. Engl. J. Med.* 359, 766–768.
- Winer, J.H., Choi, H.S., Gibbs-Strauss, S.L., Ashitate, Y., Colson, Y.L., and Frangioni, J.V. (2010). Intraoperative localization of insulinoma and normal pancreas using invisible near-infrared fluorescent light. *Ann. Surg. Oncol.* 17, 1094–1100.
- Wong, K.P., Tsang, J.S., and Lang, B.H. (2018). Role of surgery in pancreatic neuroendocrine tumor. *Gland Surg.* 7, 36–41.

iScience, Volume 23

Supplemental Information

Rapid and Selective Targeting

of Heterogeneous Pancreatic

Neuroendocrine Tumors

G. Kate Park, Jeong Heon Lee, Eduardo Soriano, Myunghwan Choi, Kai Bao, Wataru Katagiri, Do-Yeon Kim, Ji-Hye Paik, Seok-Hyun Yun, John V. Frangioni, Thomas E. Clancy, Satoshi Kashiwagi, Maged Henary, and Hak Soo Choi

TRANSPARENT METHODS

Chemicals and Methods

All chemicals and solvents were of American Chemical Society grade or HPLC purity and were used as received. HPLC grade acetonitrile (CH₃CN) and water were purchased from VWR International (West Chester, PA) and American Bioanalytic (Natick, MA), respectively. All other chemicals were purchased from Fisher Scientific (Pittsburgh, PA, USA) and Sigma-Aldrich (Saint Louis, MO). Melting points (mp, open Pyrex capillary) were measured on a Meltemp apparatus and are uncorrected. ¹H- and ¹³C-NMR spectra were recorded on a BrukerAvance (400 MHz) spectrometer. Vis/NIR absorption spectra were recorded on a Perkin Elmer Lambda 20 spectrophotometer or Varian 50 scan UV-visible spectrophotometer. Chemical purity was also confirmed using ultra-performance liquid chromatography (UPLC, Waters, Milford, MA) combined with simultaneous evaporative light scattering detection (ELSD), absorbance (photodiode array; PDA), fluorescence, and electrospray time-of-flight (ES-TOF) mass spectrometry (MS).

Synthesis of symmetrical and unsymmetrical phenoxazine derivatives: A series of phenoxazinium based dyes x-x was synthesized through the condensation reaction between a p-nitrosoanilines with substituted naphthalen-1-ols, naphthalen-1-amines or 3-aminophenols in acidic solutions, as shown in Scheme 1. The required precursor, nitrosophenol can be obtained by the usual procedure involving treatment of either di-alkylated or mono alkylated m-aminophenol with sodium nitrite in the presence of hydrochloric acid. Since nitroso reagent constitutes the first half of the dye, the alternate half has to be carefully selected since they determine the substituents present at the 5- and 9- positions of the tetracyclic system and 5- and 7- positions of the tricyclic system of the target compounds. The cyclization occurs in the presence of a strong mineral acid, such as perchloric or hydrochloric acids and is driven by the formation of the aromatic dye.

***N*-(7-(dimethylamino)-3*H*-phenoxazin-3-ylidene)-*N*-methylmethanaminium chloride (Ox61):**

A mixture of compound 3 and 5 (2 mmol) in *i*-PrOH (20 mL) was stirred under an inert atmosphere. 2 mol eq of HCl was added, and the mixture was heated under reflux for 6 h. The dark blue solution was concentrated under reduced pressure and the residue was purified by silica gel column chromatography, using acetone/methanol (from 10:1 to 10:2 v/v). The dark blue fractions were concentrated to a total volume of 2 mL, and a 1:1 mixture of EtOAc and Et₂O (20 mL) was added

to crystallize the product. The mixture was ultrasonicated for 10 min and filtered. The powder was washed with EtOAc and Et₂O then dried under reduced pressure. Yield 45%; mp 190 °C; ¹H-NMR (400 MHz, MeOD-d₄): δ ppm 3.42 (s, 12 H), 6.90 (s, 2 H), 7.37 (d, *J* = 7.07 Hz, 2 H), 7.72 (br. s., 2 H); ¹³C-NMR (100 MHz, MeOD-d₄): δ ppm 40.40, 96.12, 117.18, 133.76, 148.92, 157.90.

***N*-(7-(dimethylamino)-2-methyl-3*H*-phenoxazin-3-ylidene)ethanaminium perchlorate (Ox89):**

A mixture of 3-methoxy-*N,N*-dimethyl-4-nitrosoaniline with 2 mol eq of perchloric acid in *i*-PrOH (10 mL) was stirred at 30 °C. A solution of compound 3-(Ethylamino)-4-methylphenol in 90% *i*-PrOH (10 mL) was added dropwise to the above mixture during 45 min. The reaction was monitored via UV-Vis. The dark blue solution was evaporated, followed by purification using column chromatography with CH₂Cl₂/MeOH from 10:1 to 1:1 (v/v) and the dark blue solution was evaporated. To a solution of the residue EtOH or MeOH (2 mL), was added AcOEt (20 mL). After ultrasonication for 10 min, the mixture was filtrated. The powder was washed by AcOEt and Et₂O then dried in under reduced pressure. Yield (30%); mp: > 260 °C; ¹H-NMR (400 MHz, DMSO-*d*₆) δ ppm 7.59 (d, *J* = 9.09 Hz, 1 H), 7.42 (br. s., 1 H), 7.21 (d, *J* = 9.09 Hz, 1 H), 6.69 (br. s., 2 H), 3.50 (q, *J* = 5.81 Hz, 2 H), 3.28 (s, 6 H), 2.30 (s, 3 H), 1.27 (t, *J* = 12.8, 4 H); ¹³C-NMR (100 MHz, DMSO-*d*₆): δ ppm 157.25, 156.44, 148.52, 147.82, 134.19, 133.17, 132.64, 132.21, 129.33, 116.93, 95.96, 93.87, 41.15, 39.02, 17.42, 13.86; HRMS (TOF MS ES⁺): calcd for C₁₇H₂₀N₃O⁺: m/z 282.1601 ([M]⁺), found: m/z 282.1435 [M]⁺.

***N*-(7-(dimethylamino)-3*H*-phenoxazin-3-ylidene)-*N*-ethylethanaminium perchlorate (Ox261):**

The compound was prepared as reported previously with slight modification to method.(Ge et al., 2008) *N,N*-methyl-4-nitrosoaniline was used instead of 3-methoxy-*N,N*-dimethyl-4-nitrosoaniline for the condensation reaction. Yield (11%); mp: > 260 °C; ¹H-NMR (400 MHz, Acetone-*d*₆) δ ppm 7.83-7.85 (m, 2H, Ar-H), 7.48-7.54 (m, 2H, Ar-H), 6.97-7.02 (m, 2H, Ar-H), 3.89-3.84 (m, 4H, CH₂), 3.53 (s, 6H, CH₃), 1.40-1.44 (m, 6H, CH₃); ¹³C-NMR (100MHz, CDCl₃) δ ppm 117.6, 117.4, 96.3, 96.2, 46.5, 40.9, 21.1; HRMS (TOF MS ES⁺): calcd for C₁₈H₂₂N₃O⁺: m/z 296.3862 ([M]⁺), found: m/z 295.5393 [M]⁺.

***N*-(7-(diethylamino)-3*H*-phenoxazin-3-ylidene)-*N*-ethylethanaminium chloride (Ox96):** The compound was prepared as reported previously.(Ge et al., 2008) Yield 40%; mp: 204 °C (dec.); ¹H-

NMR (400 MHz, MeOD-d₄) δ ppm 7.81 (d, J = 8.8 Hz, 2 H), 7.41 (d, J = 8.8 Hz, 2 H), 6.98 (br. s., 2 H), 3.86 - 3.72 (m, 8 H), 1.38 (br. s., 12 H); ¹³C-NMR (100 MHz, MeOD-d₄) δ ppm 157.9, 151.0, 135.7, 118.7, 97.5, 47.8, 13.2; HRMS (TOF MS ES⁺): calcd for C₂₀H₂₆N₃O⁺: m/z 324.2070 ([M]⁺), found: m/z 324.1858 [M]⁺.

1-(7-(dimethylamino)-3*H*-phenoxazin-3-ylidene)pyrrolidin-1-ium perchlorate (Ox266): The compound was prepared as reported previously with slight modification to method.(Ge et al., 2008) *N,N*-methyl-4-nitrosoaniline was used instead of 3-methoxy-*N,N*-dimethyl-4-nitrosoaniline for the condensation reaction. Yield 5%; mp: > 260 °C; ¹H-NMR (400 MHz, DMSO-*d*₆) δ ppm 7.72 (s, 2H, Ar-H), 7.33 (d, J = 9.6 Hz, 1H, Ar-H), 7.23 (d, J = 9.2 Hz, 1H, Ar-H), 6.86 (s, 1H, Ar-H), 6.73 (s, 1H, Ar-H), 3.66-3.73 (m, 4H, CH₂), 3.33 (s, 6H, CH₃), 2.06 (s, 4H, CH₂); ¹³C-NMR (100MHz, CDCl₃) δ ppm 157.3, 154.9, 148.8, 148.6, 134.6, 134.3, 133.9, 133.5, 119.2, 117.5, 97.2, 96.7, 50.4, 50.1, 41.6 25.2, 24.9; HRMS (TOF MS ES⁺): calcd for C₁₈H₂₀N₃O⁺: m/z 294.1601 ([M]⁺), found: m/z 294.1310 [M]⁺.

1-(7-(dimethylamino)-3*H*-phenoxazin-3-ylidene)piperidin-1-ium perchlorate (Ox269): The compound was prepared as reported previously with slight modification to method.(Ge et al., 2008) *N,N*-methyl-4-nitrosoaniline was used instead of 3-methoxy-*N,N*-dimethyl-4-nitrosoaniline for the condensation reaction. Yield (15%); m.p 255-257 °C; ¹H-NMR (400 MHz, DMSO-*d*₆) δ 7.76-7.80 (s, 2H, Ar-H), 7.58-7.61 (m, 1H, Ar-H), 7.37-7.40 (m, 1H, Ar-H), 7.18-7.19 (m, 1H, Ar-H), 6.89-6.90 (m, 1H, Ar-H), 3.88-3.90 (m, 4H, CH₂), 3.41 (s, 6H, CH₃), 1.72 (s, 6H, CH₂); ¹³C-NMR (100MHz, CDCl₃) δ ppm 147.1, 145.6, 134.2, 133.1, 120.2, 116.6, 115.6, 114.7, 112.2, 110.7, 106.9, 63.6, 59.3, 56.4, 43.6, 33.3, 22.7, 21.5, 20.7, 19.7, 18.7, 12.7, 12.12; HRMS (TOF MS ES⁺): calcd for C₁₉H₂₂N₃O⁺: m/z 308.1757 ([M]⁺), found: m/z 308.1742 [M]⁺.

9-(ethylamino)-10-methyl-5*H*-benzo[*a*]phenoxazin-5-iminium chloride (Ox12): The compound was prepared as reported previously.(Frade et al., 2008, Frade et al., 2006) Yield (0.7 g, 83 %); mp: 260 °C; ¹H-NMR (D₂O, 70 °C) δ ppm 8.4 (s, 1H), 8.1 (br s, 1H), 7.9 (s, 1H), 7.3 (s, 1H), 7.2 (s, 1H), 6.7 (s, 2H), 6.5 (s, 1H), 3.73 (s, 3H), 2.36 (m, 2H), 1.64 (m, 3H); ¹³C-NMR (DMSO-*d*₆): δ ppm 161.49, 160.44, 153.63, 150.70, 146.59, 133.84, 133.72, 130.64, 127.72, 126.72, 125.04, 118.53,

114.85, 108.31, 95.26, 93.29, 37.75, 16.95, 13.48; LCMS ESI TOF: calcd for C₁₉H₁₈N₃O⁺: m/z 304.14 ([M+H]⁺), found: m/z 304.4 [M+H]⁺.

9-(diethylamino)-5*H*-pyrido[3,2-*a*]phenoxazin-5-iminium chloride (Ox17): To a round bottom flask, 5-(diethylamino)-2-nitrosophenol (2.7 mmol) and quinolin-8-amine (2.7 mmol) were dissolved in ethanol (20 mL). To the solution, concentrated HCl (0.1 mL, 37%) was added. The mixture was heated to reflux for 72 h with stirring. After heating, the reaction was cooled to room temperature with a residue obtained by filtration. The residue was then dissolved in distilled water (40 mL) and the solution was adjusted to pH~9.0 by the slow addition of ammonia. The basic mixture was stirred for 3 h at room temperature, and then filtered. Purification was achieved using silica column chromatography using CH₂Cl₂ /MeOH as the solvent system to provide the pure dye. Yield 56%; mp: 247-249 °C; ¹H-NMR (MeOD-*d*₄): δ ppm 9.12 (m, 1H), 9.02 (m, 1H), 7.85-9.05(m, 2H), 7.33 (m, 1H), 6.99 (m, 1H), 3.73 (m, 4H), 1.37 (m, 6H); ¹³C-NMR (MeOD-*d*₄): δ ppm 162.38, 161.39, 153.67, 151.54, 147.73, 134.49, 134.15, 132.33, 128.49, 125.86, 118.67, 114.78, 113.90, 108.77, 95.45, 45.40, 11.55; HRMS (TOF MS ES⁺): calcd for C₁₉H₁₉N₄O⁺: m/z 319.1553 ([M]⁺), found: m/z 319.1230 [M]⁺.

9-(ethylamino)-6,10-dimethyl-5*H*-benzo[*a*]phenoxazin-5-iminium chloride (Ox14): The 2-methylnaphthalen-1-amine was dissolved in ethanol and cooled to 0 °C. To this was added 5-(ethylamino)-4-methyl-2-nitrosophenol and conc. HCl (0.05 mL). The mixture was refluxed for 3.5 h and monitored by TLC using CH₂Cl₂ and MeOH as solvent. After complete conversion of the starting materials, the reaction was quenched by adding 5% NaHCO₃ and extracted with ethyl acetate. Purification was achieved using silica gel column chromatography using CH₂Cl₂/MeOH (9/1) as the solvent system to provide the pure dye. Yield (0.83 g, 73 %); mp: 225-230 °C; ¹H-NMR (D₂O, 70 °C) δ ppm 7.86 (s, 1H), 7.67 (s, 3H), 6.63 (s, 1H), 5.93 (s, 1H), 3.28 (s, 2H), 2.06 (s, 3H), 1.87 (s, 3H), 1.52 (s, 3H); ¹³C-NMR (MeOD) δ ppm 176.00, 157.09, 131.53, 131.10, 129.00, 123.44, 122.24, 121.14, 95.83, 48.45, 37.51, 16.08, 12.74; HRMS (TOF MS ES⁺): calcd for C₂₀H₂₀N₃O⁺: m/z 318.16 ([M]⁺), found: m/z 318.1 [M]⁺.

9-(ethylamino)-2-hydroxy-10-methyl-5*H*-benzo[*a*]phenoxazin-5-iminium chloride (Ox13): The compound was prepared as reported previously.(Firmino et al., 2014) Yield (0.83 g, 73%); mp:

255 – 260 °C; ¹H-NMR (DMSO-*d*₆, 70 °C) δ ppm 10.94 (br s, 1H), 9.70 (br s, 1H), 8.39 – 8.37 (d, *J* = 8.0 Hz, 1H), 8.09 (s, 1H), 7.57 (s, 1H), 7.32 – 7.25 (m, 2H), 6.81 – 6.78 (m, 1H), 3.43 (s, 2H), 2.27 (s, 3H), 1.27 (s, 3H); ¹³C-NMR (DMSO-*d*₆): 162.30, 161.26, 154.44, 151.50, 147.39, 134.66, 131.44, 127.51, 125.85, 119.34, 115.63, 109.13, 96.09, 94.09, 49.03, 38.55, 17.71, 14.26; LCMS ESI TOF: calcd for C₅₀H₆₅N₄O₈S₃⁺: *m/z* 946.4031([M+H]⁺), found: *m/z* 473.1717 [M+H]²⁺. Lit. mp: >300 °C.

9-(diethylamino)-2-hydroxy-5*H*-benzo[*a*]phenoxazin-5-iminium chloride (Ox16): The compound was prepared as reported previously.(Liu et al., 2014) Yield (43%). mp: >260 °C ¹H-NMR (DMSO-*d*₆): δ ppm 11.05 (s, 1H), 9.12 (brs, 1H), 9.79 (s, 1H), 8.37 (d, *J* = 9Hz, 1H), 8.12 (s, 1H), 7.79 (d, *J* = 9 Hz, 1H), 7.27 (m, 1H), 7.16 (m, 1H), 6.96 (s, 1H), 6.76 (s, 1H), 3.64 (m, 4H), 1.22 (m, 6H), ¹³C-NMR (MeOD-*d*₄): δ ppm 162.38, 161.39, 153.67, 151.54, 147.73, 134.49, 134.15, 132.33, 128.49, 125.86, 118.67, 114.78, 113.90, 108.77, 95.45, 45.40, 11.55; HRMS (TOF MS ES⁺): calcd for C₂₀H₂₀N₃O₂⁺ : *m/z* 334.1550 ([M]⁺), found: *m/z* 334.1465 [M]⁺; Lit. Yield: 50.5%, mp: >300 °C.

dimethyl-3,3'-((5-oxo-5*H*-benzo[*a*]phenoxazine-9-yl)azanediyl)dipropionate (Ox34): The compound was prepared as reported previously.(Jose and Burgess, 2006) mp: > 260 °C; ¹H-NMR (DMSO-*d*₆): δ ppm 10.54 (s, 1H), 7.96 (d, *J* = 8.8 Hz, 1H), 7.88 (s, 1H), 7.59 (d, *J* = 9.2 Hz, 1H), 7.09 (dd, 1H), 6.81 (dd, 1H), 6.70 (d, *J* = 2.4 Hz, 1H), 6.15 (s, 1H), 3.73 (t, *J* = 7.2 Hz, 4H), 3.62 (s, 1H), 2.652 (t, *J* = 7.2 Hz, 4H); ¹³C-NMR (DMSO-*d*₆): δ ppm 181.68, 171.74, 160.69, 151.48, 150.19, 146.11, 139.98, 133.61, 130.70, 127.50, 124.27, 123.85, 118.59, 110.06, 108.30, 104.42, 96.98, 51.53, 46.30, 31.46; LCMS ESI TOF: calcd for C₂₄H₂₂N₂O₇⁺: *m/z* 473.1319 ([M+Na]⁺), found: *m/z* 473.1456 [M+Na]⁺; Lit. Yield: 60%.

9-(bis(3-methoxy-3-oxopropyl)amino)-2-hydroxy-5*H*-benzo[*a*]phenoxazin-5-iminium chloride (Ox37): To a round bottom flask, 6-aminonaphthol (2.7 g, 16.9 mmol) was added to a solution of dimethyl-3,3'-((3-hydroxy-4-nitrosophenyl)azanediyl)dipropionate (5.24 g, 16.9 mmol) in DMF (20 mL). The reaction mixture was refluxed for 3 h. The solvent was evaporated, and the residue was purified by column chromatography using CH₂Cl₂ /MeOH as the solvent system to afford the compound. mp: > 260 °C; ¹H-NMR (DMSO-*d*₆) δ ppm 11.14 (s, 1H), 10.13 (br s, 2H),

8.41 (d, $J = 8.8$ Hz, 1H), 8.11 (s, 1H), 7.81 (t, $J = 5.6$ Hz, 1H), 7.29 (d, $J = 8.8$ Hz, 1H), 7.16 (br s, 1H), 7.02 (s, 1H), 6.79 (s, 1H), 3.84 (t, $J = 6.4$ Hz, 4H), 3.63 (s, 6H), 2.72 (t, $J = 7.2$ Hz, 4H); HRMS (TOF MS ES⁺): calcd for C₂₄H₂₄N₃O₆⁺: m/z 450.1660 ([M]⁺), found: m/z 450.1071 [M]⁺.

9-(ethylamino)-2-methoxy-10-methyl-5*H*-benzo[*a*]phenoxazin-5-iminium chloride (Ox116):

To a clean dried 50 mL round bottom flask, 6-Methoxynaphthalen-1-amine (0.38 g, 2.1 mmol) was dissolved in ethanol and cooled to 0 °C. To this was added 5-(ethylamino)-4-methyl-2-nitrosophenol (0.45 g, 2.0 mmol) and conc. HCl (0.05 mL). The mixture was refluxed for 5 h and monitored by TLC using CH₂Cl₂/MeOH as solvent. After complete conversion of the starting materials, the reaction was quenched by adding 5% NaHCO₃ and extracted with ethyl acetate. Purification was achieved using silica gel column chromatography with the solvent system CH₂Cl₂/MeOH (9/1) to provide the pure compound. Yield (0.52 g, 70 %); mp: > 260 °C; ¹H-NMR (MeOD) δ ppm 8.27 – 8.21 (d, $J = 8.0$ Hz, 1H), 7.62 – 7.60 (d, $J = 2.0$ Hz, 1H), 7.39 – 7.33 (m, 2H), 6.75 (s, 1H), 5.85 (s, 1H), 4.04 (s, 1H), 2.32 (s, 3H), 1.36 (s, 7H); ¹³C-NMR (DMSO-*d*₆) δ ppm 161.97, 157.60, 154.70, 151.46, 147.59, 133.35, 133.16, 131.47, 129.29, 126.64, 126.26, 118.55, 117.54, 105.62, 93.70, 92.53, 56.19, 38.61, 17.84, 14.23; HRMS (TOF MS ES⁺): calcd for C₂₀H₂₀N₃O₂⁺: m/z 334.15 ([M]⁺), found: m/z 334.1 [M]⁺.

(*E*)-*N*-(9-(ethylamino)-2-methoxy-10-methyl-5*H*-benzo[*a*]phenoxazin-5-ylidene)methan

aminium chloride (Ox117): To a clean dried 50 mL round bottom flask, 6-methoxy-*N*-methylnaphthalen-1-amine (0.25 g, 1.33 mmol) was dissolved in ethanol and cooled to 0 °C. To this solution was added 5-(ethylamino)-4-methyl-2-nitrosophenol (0.29 g, 1.33 mmol) and conc. HCl (0.05 mL). The mixture was refluxed for 5 h and monitored by TLC using CH₂Cl₂ and MeOH as solvent. After complete conversion of the starting materials, the reaction was quenched by adding 5 % NaHCO₃ and extracted with ethyl acetate. Purification was achieved using silica gel column chromatography with the solvent system CH₂Cl₂/MeOH (9/1) to provide the pure compound. Yield (0.32 g, 70%); mp: 220-225 °C; ¹H-NMR (DMSO) δ ppm 10.19 (br s, 1H), 8.45 – 8.43 (d, $J = 8.0$ Hz, 1H), 7.82 (s, 1H), 7.62 (s, 1H), 7.44 (s, 1H), 7.28 – 7.26 (d, 1H), 6.60 – 6.54 (m, 2H), 3.92 (s, 2H), 3.17 (s, 3H), 2.22 (s, 3H), 1.28 – 1.25 (t, 3H); ¹³C-NMR (DMSO) δ ppm 161.97, 157.40, 154.70, 151.46, 147.59, 133.35, 133.16, 131.47, 129.29, 126.64, 126.26, 118.55, 117.54, 105.62,

93.70, 92.53, 56.19, 38.61, 31.64, 17.84, 14.23; HRMS (TOF MS ES⁺): calcd for C₂₁H₂₂N₃O₂⁺: m/z 348.17 ([M]⁺), found: m/z 334.1 [M]⁺.

3-((9-(diethylamino)-5-iminio-5*H*-benzo[*a*]phenoxazin-3-yl)oxy)propane-1-sulfonate (Ox27):

To a round bottom flask, 5-(diethylamino)-2-nitrosophenol (2.7 mmol) and the appropriate 5-aminonaphthalene (2.7 mmol) were dissolved in ethanol (20 mL). To the solution, concentrated HCl (0.1 mL, 37%) was added. The mixture was heated to reflux for 72 h with stirring. After heating, the reaction was cooled to room temperature with a residue obtained by filtration. The residue was then dissolved in distilled water (40 mL) and the solution was adjusted to pH~9 by the slow addition of ammonia. The basic mixture was stirred for 3 h at room temperature, and then filtered. Purification was achieved using silica column chromatography using CH₂Cl₂/MeOH as the solvent system to provide the pure dye. Yield (13%); mp: >260 °C; ¹H-NMR (DMSO-*d*₆): δ ppm 10.66 (br s, 1H), 10.35 (br s, 1H), 8.68 (d, *J* = 9 Hz, 1H), 7.83 (m, 2H), 7.44 (m, 1H), 7.22 (m, 1H), 7.10 (s, 1H), 6.94 (s, 1H), 3.86 (m, 2H), 3.63 (m, 4H), 2.65 (m, 2H), 2.07 (m, 2H), 1.22 (m, 6H); ¹³C-NMR (DMSO-*d*₆): δ ppm 161.64, 159.97, 153.01, 151.10, 147.79, 135.24, 132.33, 128.98, 126.74, 125.14, 123.98, 122.33, 114.83, 109.54, 97.32, 96.23, 45.55, 13.00; HRMS (TOF MS ES⁺): calcd for C₂₃H₂₅N₃NaO₅S⁺: m/z 478.1407 ([M+Na]⁺), found: m/z 478.1204 [M+Na]⁺.

Protein conjugation with ZW800-1: Cyclic pentapeptide cyclo (Arg-Gly-Asp-DTyr-Lys; cRGD; MW 619.6) was synthesized as previously reported, and conjugated to ZW800-1 using *N*-hydroxysuccinimide (NHS) ester chemistry in DMSO.(Choi et al., 2010) NIR fluorophores were also conjugated to GLP-1 (Abcam, Cambridge, MA) in PBS, pH 7.8, followed by purification by gel filtration chromatography. *In silico* calculations of the partition coefficient (log*D*) and surface molecular charge and hydrophobicity were calculated using MarvinSketch 5.2.1 (ChemAxon, Budapest, Hungary).

Optical and physicochemical property analyses

All optical measurements were performed at 37 °C in PBS, pH 7.4 or 100% FBS buffered with 50 mM HEPES, pH 7.4. Absorbance and fluorescence emission spectra of the series of NIR fluorophores were measured using fiber optic HR2000 absorbance (200–1100 nm) and USB2000FL fluorescence (350–1000 nm) spectrometers (Ocean Optics, Dunedin, fL). NIR excitation was provided by a 655 nm red laser pointer (Opcom Inc., Xiamen, China) set to 5 mW and coupled through a 300 μ m core diameter, NA 0.22 fiber (Fiberguide Industries, Stirling, NJ). For fluorescence quantum yield (QY) measurements, oxazine 725 in ethylene glycol (QY = 19%) was used as a calibration standard, under conditions of matched absorbance at 655 nm. *In silico* calculations of the partition coefficient (Log*D* at pH 7.4), surface molecular charge, hydrophobicity, hydrogen bond acceptors/donors (HBA/HBD), and total polar surface area (TPSA) were calculated using Marvin and JChem calculator plugins (ChemAxon, Budapest, Hungary).

Cell membrane binding assay

NIT-1 (ATCC, Manassas, VA) were seeded onto 16-well plates and incubated at 37°C in humidified 5% CO₂ incubator in F12K and DMEM, respectively, supplemented with 10% FBS and 1% Pen/Strep. When cells reached \approx 80% confluence, they were rinsed twice with PBS then MB or Ox61 was added to each well at a concentration of 2 μ M and incubated for 1 h at 37°C in a humidified 5% CO₂ incubator. Cells were washed 3 times with culture media prior to imaging. After imaging, periodic acid at a concentration of 0.1 mM was added and images were taken immediately after. The cells were observed on a 4-channel NIR fluorescence microscope. The excitation and emission filter used for microscopy was 650 \pm 22 nm and 710 \pm 25 nm, respectively.

Plasma protein binding test

The RED device was purchased from Thermo Fisher (Waltham, MA) and the plasma protein binding assay was performed following the detailed instruction provided by the manufacture. (Brouwer et al., 2000) 200 μ L of samples were prepared in mouse plasma serum at 10 μ M. The samples were added into the sample chamber and 400 μ L of PBS buffer (pH 7.4) was added to the buffer chamber. The plate was sealed with sealing tape and incubated at 37°C on a shaker at 150 rpm for 4 h. Equal volume from both the buffer and the plasma chambers were collected for samples analysis.

Fluorescence signals of each chamber were measured to calculate the percentage of bound and unbound fractions for each sample.

NIR fluorescence imaging system

For the NIR fluorescence imaging, the FLARE system has been described in detail previously.(Choi et al., 2013, Gioux et al., 2010) In this study, a 670 nm excitation was used at a fluence rate of 2 mW/cm², with white light (400 – 650 nm) at 12,000 lx. Color and NIR fluorescence images were acquired simultaneously with custom software at rates up to 15 Hz over a 10 cm diameter field-of-view (FOV). A pseudo-colored lime green was used for NIR fluorescence in the color-NIR merged images. The imaging system was positioned at a distance of 9 inches from the surgical field. For all real-time intraoperative imaging, a standardized imaging protocol was used during and after the operation. General FOV (5 cm in dia.) was used to include pancreas head, duodenum, liver, and kidneys of a mouse, while closeup FOV (3.3 cm in dia.) includes pancreas head and duodenum. Color and NIR fluorescence images were taken simultaneously.

Animal models and intraoperative fluorescence imaging

Animals were housed in an AAALAC-certified facility. Animal studies were performed under the supervision of BIDMC IACUC in accordance with approved institutional protocols (#101-2011). 4 wk old insulinoma-bearing NOD/ShiLt-Tg(RipTag)1Lt/J mice (both male and female) were purchased from Jackson Laboratories (Bar Harbor, ME). Insulinoma-bearing mice were maintained on a high glucose diet (8.4 g sugar in 250 mL water) until they were ready for intraoperative tumor targeting study. Animals were anesthetized with 100 mg/kg ketamine and 10 mg/kg xylazine intraperitoneally (Webster Veterinary, Fort Devens, MA). Following anesthesia, a midline incision was made to expose the abdominal cavity and head of the pancreas. For kinetics and dose-response studies, 0.3 to 6.0 mg/kg of MB or Ox61 in saline were injected intravenously into insulinoma-bearing tumor mice, and images were taken over 4 h (n = 5, mean ± s.d.). Control images were acquired prior to injecting NIR fluorophores. The fluorescence signal in tumors (Tu) and tumor-to-background ratio (TBR) compared to neighboring pancreas (Pa) was obtained over the period of imaging. For tumor stage targeting, insulinoma-bearing mice from 5 to 13 wk old were administered with 0.3-6.0 mg/kg of Ox61 in saline. Real-time signal accumulation at tumor site was observed over 30 min post-injection of 1.5 mg/kg of Ox61, and the fluorescence intensity was plotted to

evaluate *in vivo* molecular biodistribution and clearance. Animals were sacrificed 1-4 h post-injection, and pancreas and tumorous tissues were resected for *ex vivo* imaging and histology.

***In vivo* biodistribution and clearance**

Before the surgery, mice were anesthetized with ketamine (100 mg/kg) and xylazine (10 mg/kg) through intraperitoneal injection. Midline incision was performed to open abdominal cavity. For all real-time tumor imaging, a standardized imaging protocol was used during and after the operation. General FOV included pancreas head, duodenum, liver, and kidney. 1.5 mg/kg of MB and Ox61 were injected intravenously into 25 g male CD-1 mice, and images were taken for 4 h.

Magnetic Resonance Imaging (MRI)

1T micro MRI scanner (Aspect, Israel) was used to track tumor growth noninvasively and longitudinally.(Kim et al., 2013) Insulinoma-bearing mice were scanned once every week starting at 5 wk to 14 wk old of age. In order to optimize the MR protocol, T1-weighted spin echo, T2-weighted spin echo, and gradient echo sequences were compared using the same insulinoma-bearing mouse. T2-weighted fast-spin echo (FSE) sequence was used to localize tumor with echo time (TE) of 80 ms and repetition time (TR) of 4,000 ms using 4 NEX, 256 x 256 matrix, and 1 mm slice thickness. MRI images were analyzed using VivoQuant 1.22 software.

Histology and immunohistochemistry (IHC)

Pancreas was embedded in Tissue-Tek OCT compound (Fisher Scientific) without a pre-fixation step and the tissue solidified at – 80°C. Frozen samples were cryosectioned (10 µm per slice) and fixed in acetone; 1 slide was stained with H&E and consecutive sections were used for fluorescence microscopy and IHC. For IHC, Exendin-4 (GLP-1 agonist; Abcam) conjugated with ZW800-1 was used to visualize pancreatic islet cell tumors. Fluorescence imaging was conducted using a Nikon TE2000 epifluorescence microscope equipped with a 75 W xenon light source, NIR-compatible optics, and a NIR-compatible 4X, 10X, 20X, and 40X Plan Fluor objective lens (Nikon, Melville, NY). Images were acquired on an Orca-AG (Hamamatsu, Bridgewater, NJ). Image acquisition and analysis was performed using IPLab software (Scanalytics, Fairfax, VA). A custom filter set (Chroma Technology Corporation, Brattleboro, VT) composed of a 650/45 nm excitation filter, a 685 nm dichroic mirror, and a 720/60 nm emission filter were used for imaging.

Quantitative analysis

At each time point, the fluorescence and background intensity of a region of interest (ROI) over each tissue was quantified using custom FLARE software. The signal-to-background ratio (SBR) was calculated as $SBR = \text{target signal}/\text{background signal}$, where background is surrounding tissue. The TBR was calculated as tumor fluorescence/background signal, where background is the signal intensity of neighboring pancreas obtained over the imaging period. All NIR fluorescence images were normalized identically for all conditions of an experiment. At least 5 animals were analyzed at each experimental condition. Statistical analysis was carried out using a one-way ANOVA followed by Tukey's multiple comparisons test. P values less than 0.05 were considered significant: $*P < 0.05$, $**P < 0.01$, and $***P < 0.001$. The experiments were not randomized, and the investigators were not blinded to allocation during experiments and outcome assessment. Results were presented as mean \pm s.d. and curve fitting was performed using Microsoft Excel and Prism version 4.0a software (GraphPad, San Diego, CA).

Intravital laser-scanning microscopy

Under ketamine-xylazine anesthesia, the insulinoma-bearing mice were mounted on a heated stage. The pancreas was placed under the upright water immersion objective lens (20X, 1.0 NA) of a custom-built, video-rate (30 Hz), laser-scanning two-photon microscope. Both FITC-dextran (2 MDa MW) and Ox61 were excited by 150 fs pulses centered at 800 nm from a Ti:Sapphire laser. The average power was tuned to ~ 20 mW at the sample. The microscope has 3 simultaneous detection channels comprising dielectric optical filters and photomultiplier tubes. The two-photon excited fluorescence from Ox61 was collected with a band-pass filter at 600 ± 50 nm, and the fluorescence from FITC-dextran was detected with a 525 ± 25 nm filter. Images were acquired by averaging 30 video frames (1 s). The images were analyzed using ImageJ version 1.45q software.

REFERENCES

- Brouwer, E., Verweij, J., De Bruijn, P., Loos, W. J., Pillay, M., Buijs, D. & Sparreboom, A. 2000. Measurement of fraction unbound paclitaxel in human plasma. *Drug Metab Dispos*, 28, 1141-5.
- Choi, H. S., Gibbs, S. L., Lee, J. H., Kim, S. H., Ashitate, Y., Liu, F., Hyun, H., Park, G., Xie, Y., Bae, S., Henary, M. & Frangioni, J. V. 2013. Targeted zwitterionic near-infrared fluorophores for improved optical imaging. *Nat. Biotechnol.*, 31, 148-53.
- Choi, H. S., Liu, W., Liu, F., Nasr, K., Misra, P., Bawendi, M. G. & Frangioni, J. V. 2010. Design considerations for tumour-targeted nanoparticles. *Nat Nanotechnol*, 5, 42-7.
- Firmino, P. R., Mattos Neto, P. S. & Ferreira, T. A. 2014. Correcting and combining time series forecasters. *Neural Netw*, 50, 1-11.
- Frade, V. H., Sousa, M. J., Moura, J. C. & Goncalves, M. S. 2008. Synthesis of naphtho[2,3-a]phenoxazinium chlorides: structure-activity relationships of these heterocycles and benzo[a]phenoxazinium chlorides as new antimicrobials. *Bioorg Med Chem*, 16, 3274-82.
- Frade, V. H. J., Goncalves, M. S. T., Coutinho, P. J. G. & João, C. V. P. 2006. Synthesis and spectral properties of long-wavelength fluorescent dyes. *Journal of Photochemistry and Photobiology A: Chemistry*, 185, 220-230.
- Ge, J. F., Arai, C., Kaiser, M., Wittlin, S., Brun, R. & Ihara, M. 2008. Synthesis and in vitro antiprotozoal activities of water-soluble, inexpensive 3,7-bis(dialkylamino)phenoxazin-5-ium derivatives. *J Med Chem*, 51, 3654-8.
- Gioux, S., Choi, H. S. & Frangioni, J. V. 2010. Image-guided surgery using invisible near-infrared light: fundamentals of clinical translation. *Mol. Imaging*, 9, 237-55.
- Jose, J. & Burgess, K. 2006. Syntheses and Properties of Water-Soluble Nile Red Derivatives. *The Journal of Organic Chemistry*, 71, 7835-7839.
- Kim, S. H., Lee, J. H., Hyun, H., Ashitate, Y., Park, G., Robichaud, K., Lunsford, E., Lee, S. J., Khang, G. & Choi, H. S. 2013. Near-infrared fluorescence imaging for noninvasive trafficking of scaffold degradation. *Sci Rep*, 3, 1198.
- Liu, X. D., Fan, C., Sun, R., Xu, Y. J. & Ge, J. F. 2014. Nile-red and Nile-blue-based near-infrared fluorescent probes for in-cellulo imaging of hydrogen sulfide. *Anal Bioanal Chem*, 406, 7059-70.

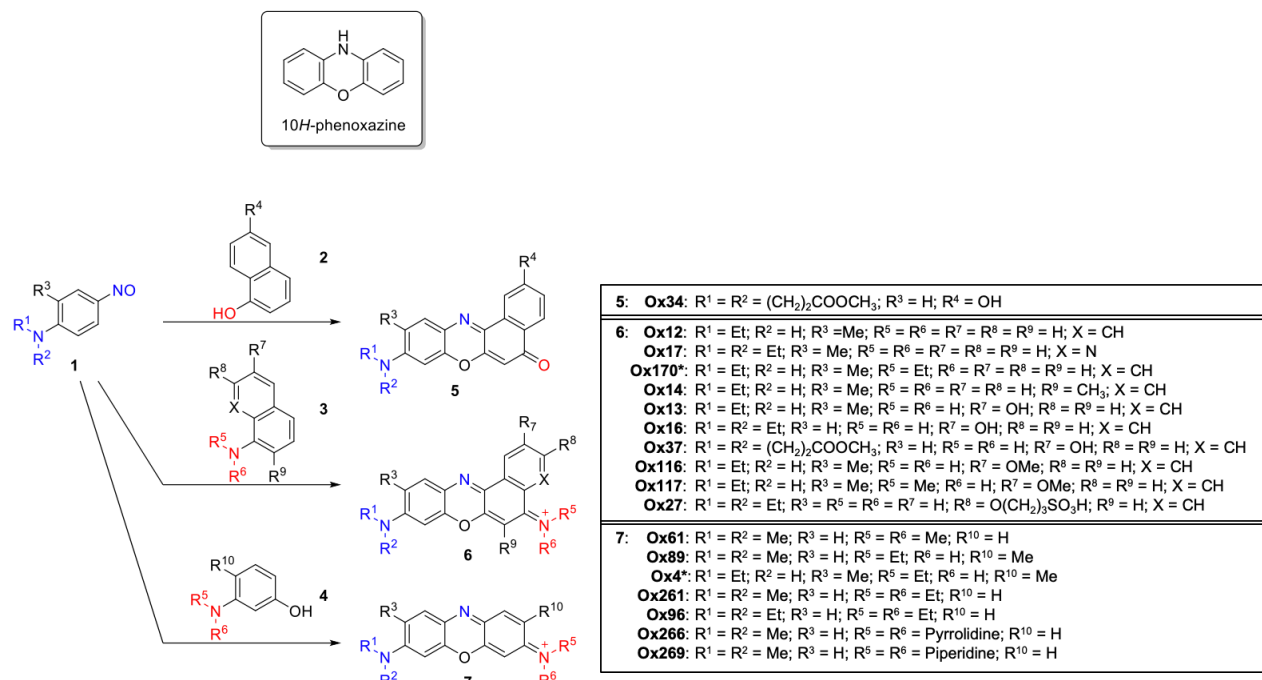
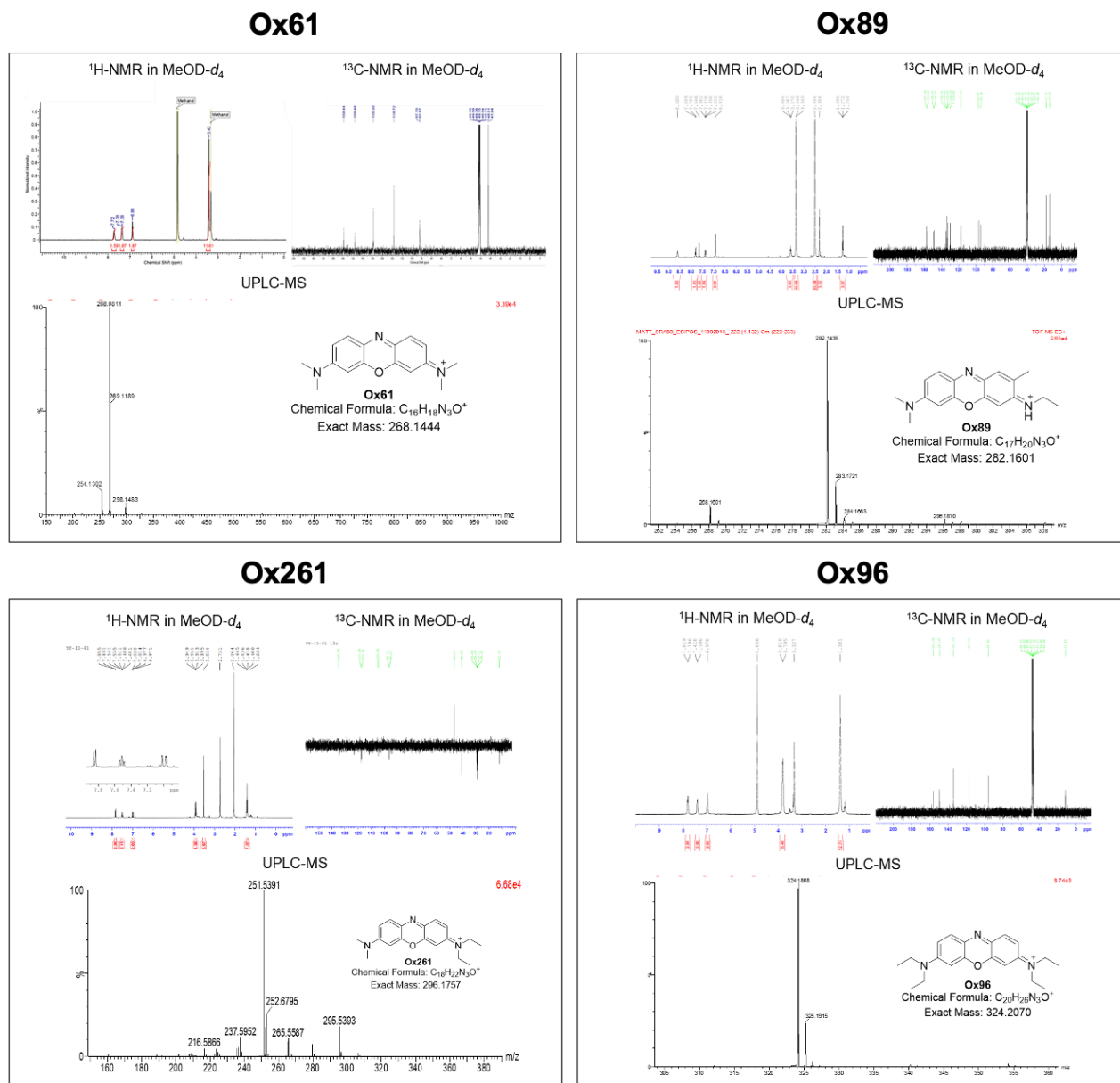


Figure S1. Related to Figure 1. Chemical synthesis of symmetrical and unsymmetrical phenoxazine derivatives. *Commercially available compounds.



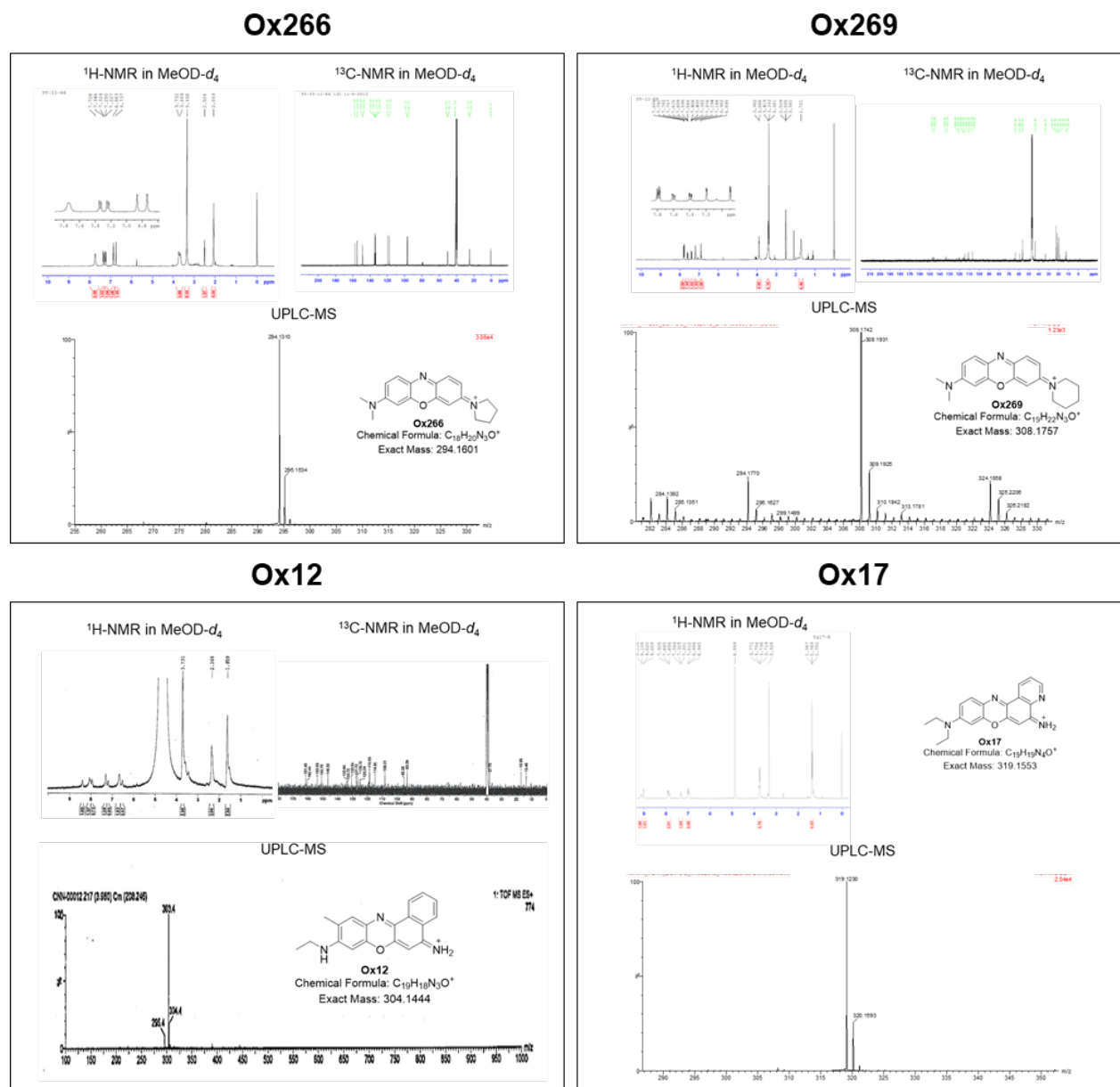


Figure S3. Chemical analysis of Ox derivatives, Related to Figure 1. $^1\text{H-NMR}$, $^{13}\text{C-NMR}$, and LC-MS analysis of phenoxazine derivatives: absorbance (photodiode array; PDA) at 210 nm, fluorescence (FLD; $\lambda_{\text{Exc}} = 648 \text{ nm}$ and $\lambda_{\text{Em}} = 668 \text{ nm}$), and electrospray time-of-flight (ES-TOF) mass spectrometry (MS).

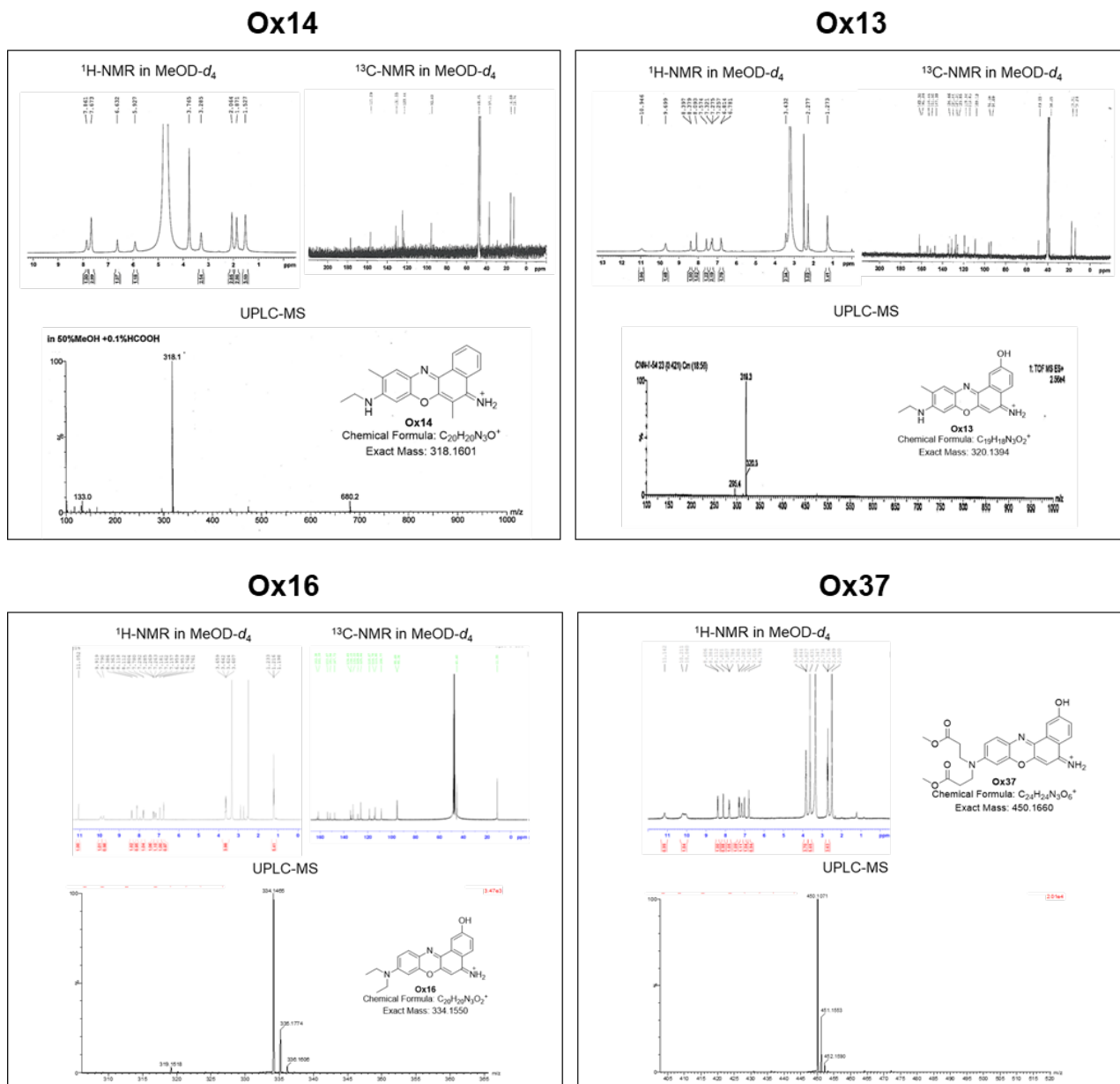


Figure S4. Chemical analysis of Ox derivatives, Related to Figure 1. $^1\text{H-NMR}$, $^{13}\text{C-NMR}$, and LC-MS analysis of phenoxazine derivatives: absorbance (photodiode array; PDA) at 210 nm, fluorescence (FLD; $\lambda_{\text{Exc}} = 648 \text{ nm}$ and $\lambda_{\text{Em}} = 668 \text{ nm}$), and electrospray time-of-flight (ES-TOF) mass spectrometry (MS).

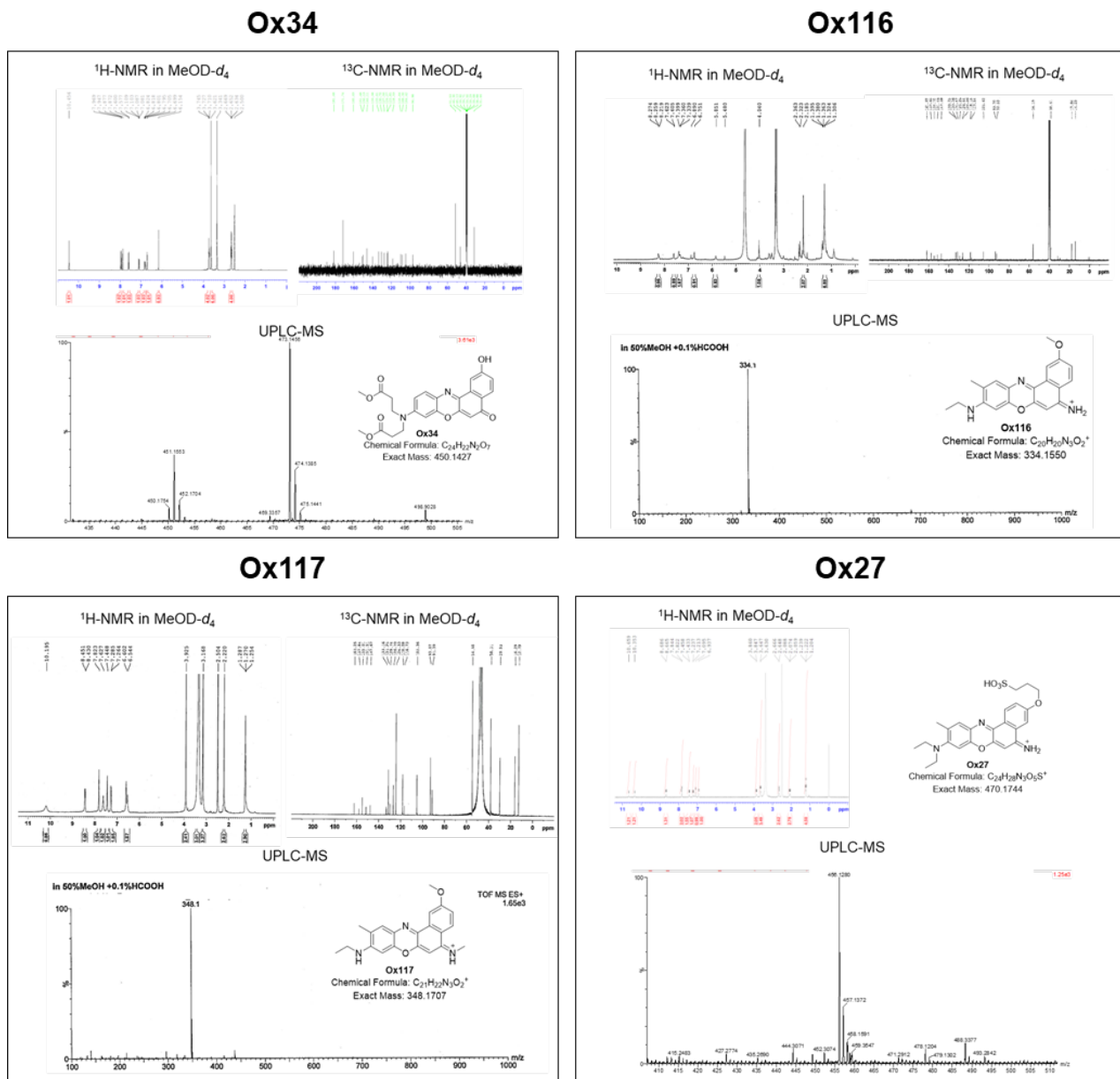


Figure S5. Chemical analysis of Ox derivatives, Related to Figure 1. $^1\text{H-NMR}$, $^{13}\text{C-NMR}$, and LC-MS analysis of phenoxazine derivatives: absorbance (photodiode array; PDA) at 210 nm, fluorescence (FLD; $\lambda_{\text{Exc}} = 648 \text{ nm}$ and $\lambda_{\text{Em}} = 668 \text{ nm}$), and electrospray time-of-flight (ES-TOF) mass spectrometry (MS).

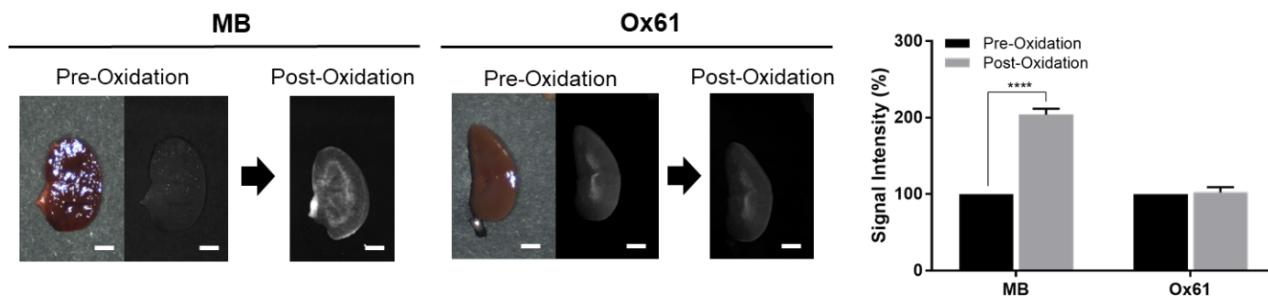


Figure S6. *Ex vivo* imaging of kidneys resected from CD-1 mice injected with 1.5 mg/kg of MB or Ox61, Related to Figure 1D. The same kidney sections were imaged again after treating with 1 mM of periodic acid and signal intensity of pre- and post-oxidation were compared ($P < 0.0001$). Scale bars = 2 mm.

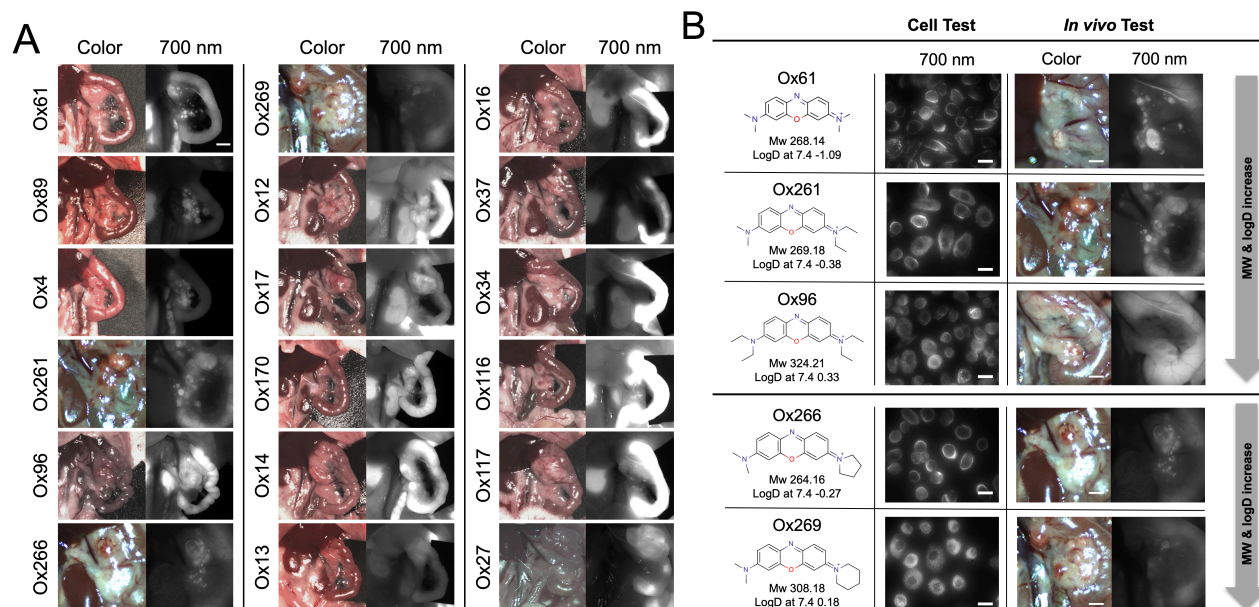


Figure S7. Tumor targetability of Ox derivatives in insulinoma mice, Related to Figure 3. (A) 1.5 mg/kg of Ox derivatives are injected intravenously into 13 wk old insulinoma mice and imaged 30 min post-injection. Scale bars = 3 mm. (B) Increase in molecular weight and logD by elongation of the side chain effects tumor targetability. Scale bars = 50 μ m.

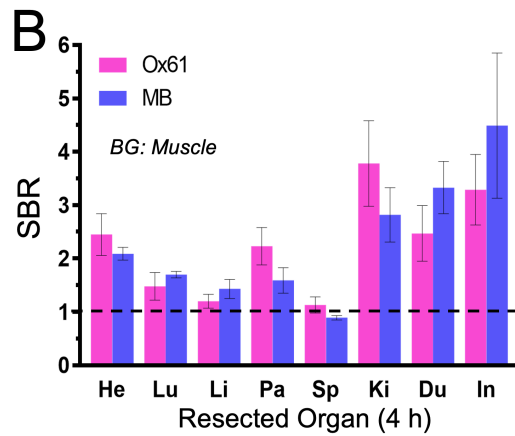
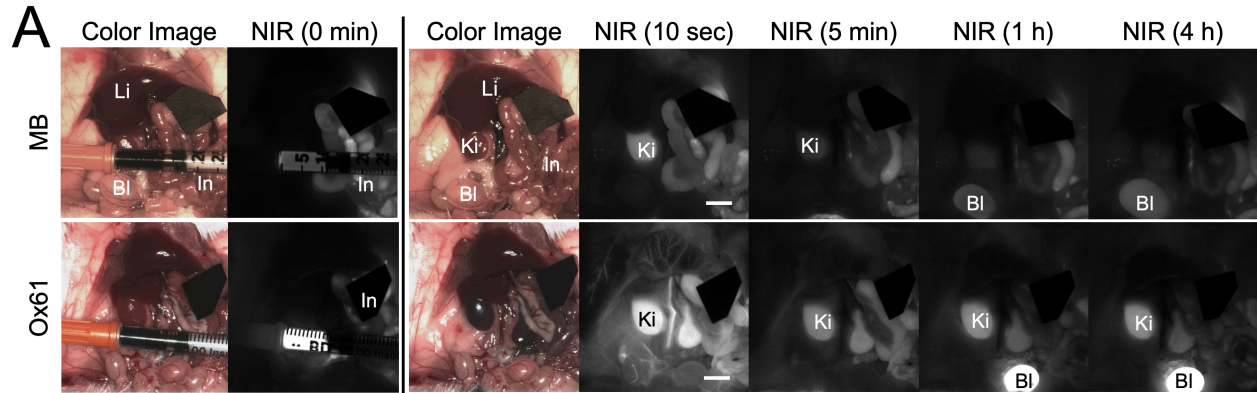


Figure S8. Kinetics optimization of MB and Ox61 in CD-1 mice, Related to Figure 3. (A) Intraoperative biodistribution of MB and Ox61. Scale bars = 5 mm. **(B)** Resected organs were imaged 4 h post-injection and SBR was quantified against muscle. SBR, signal-to-background ratio; He, heart; Lu, lung; Li, liver; Pa, pancreas; Sp, spleen; Ki, kidney, Du; duodenum; and In, intestine.

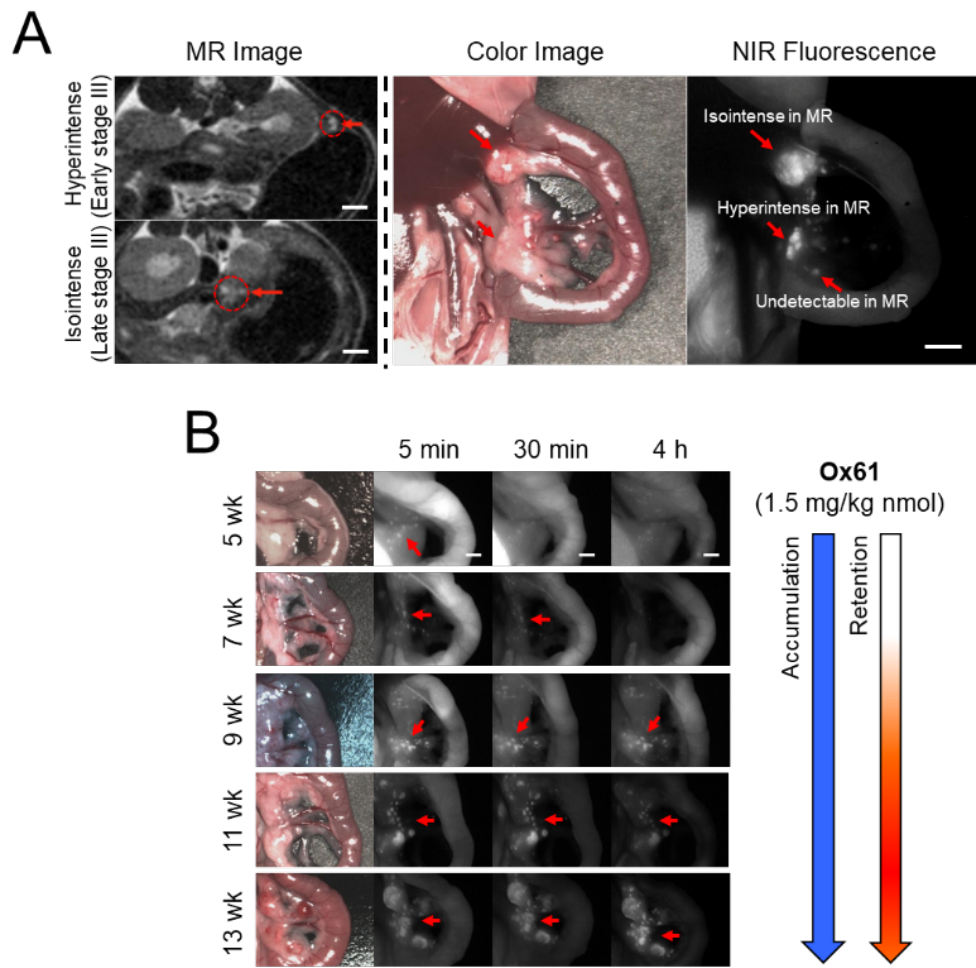


Figure S9. Intraoperative imaging of insulinomas in different stage of insulinomas, Related to Figure 3. **(A)** MR tracking and co-registration of isointense and hyperintense tumors using NIR fluorescence imaging after a single bolus injection of Ox61 (1.5 mg/kg) into insulinoma-bearing tumor mice. **(B)** Insulinoma mice from ages 5 to 13 wk were injected with 1.5 mg/kg of Ox61 and imaged 5, 30 min and 4 h post-intravenous injection. Scale bars = 3 mm.

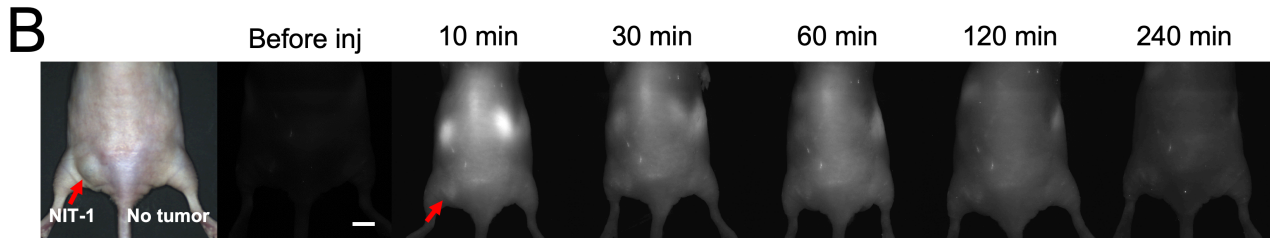
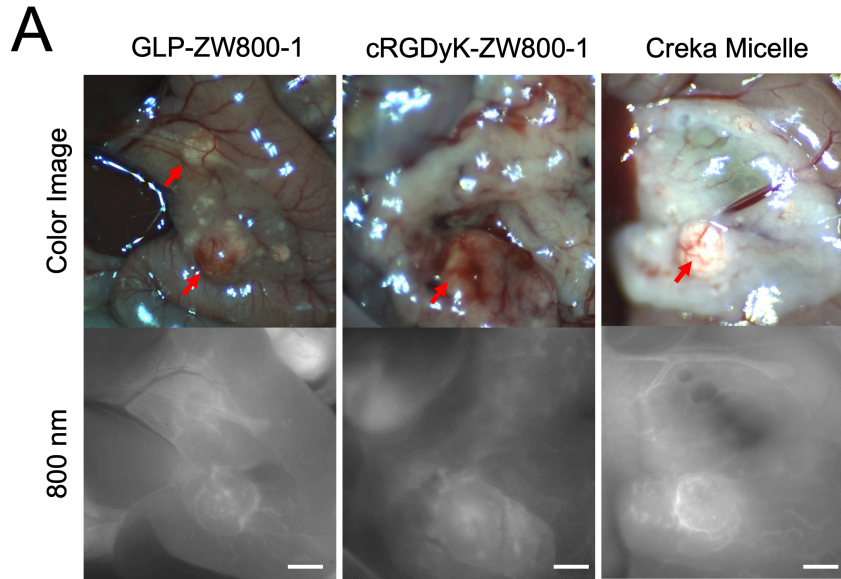


Figure S10. Intraoperative tumor targeting using ZW800-1-conjugated peptides or proteins, Related to Figure 4. **(A)** ZW800-1-conjugated GLP-1, cRGD or CREKA micelles were injected intravenously into insulinoma mice 1 h prior to imaging. Scale bars = 2 mm. **(B)** Nude mice with NIT-1 subcutaneous tumors were injected with 1.5 mg/kg of Ox61 and imaged up to 4 h. Scale bar = 5 mm.